



HAL
open science

Constraining Alteration Processes Along the Siccar Point Group Unconformity, Gale Crater, Mars: Results from the Sample Analysis at Mars Instrument

Brad Sutter, A.C. Mcadam, G.M. Wong, J.V. Clark, P.D. Archer, H.B. Franz, P.J. Gasda, D.W. Ming, A. Yen, J.M.T. Lewis, et al.

► **To cite this version:**

Brad Sutter, A.C. Mcadam, G.M. Wong, J.V. Clark, P.D. Archer, et al.. Constraining Alteration Processes Along the Siccar Point Group Unconformity, Gale Crater, Mars: Results from the Sample Analysis at Mars Instrument. *Journal of Geophysical Research. Planets*, 2022, 22 (11), pp.e2022JE007387. 10.1029/2022JE007387 . insu-03850018

HAL Id: insu-03850018

<https://insu.hal.science/insu-03850018>

Submitted on 1 Dec 2022

HAL is a multi-disciplinary open access archive for the deposit and dissemination of scientific research documents, whether they are published or not. The documents may come from teaching and research institutions in France or abroad, or from public or private research centers.

L'archive ouverte pluridisciplinaire **HAL**, est destinée au dépôt et à la diffusion de documents scientifiques de niveau recherche, publiés ou non, émanant des établissements d'enseignement et de recherche français ou étrangers, des laboratoires publics ou privés.



Distributed under a Creative Commons Attribution - NonCommercial 4.0 International License

†Deceased 28 January 2021

Special Section:

The Curiosity rover's investigation of Glen Torridon and the surrounding area

Key Points:

- Subsurface silica-poor brines or acidic fluids altered mudstones just below the Siccar Point group unconformity
- Stimson formation sandstone above the unconformity was exposed to limited aqueous alteration
- Aqueous alteration processes along the unconformity could have provided habitable conditions and in some cases, sufficient microbial C and N

Supporting Information:

Supporting Information may be found in the online version of this article.

Correspondence to:B. Sutter,
brad.sutter-2@nasa.gov**Citation:**

Sutter, B., McAdam, A. C., Wong, G. M., Clark, J. V., Archer, P. D., Franz, H. B., et al. (2022). Constraining alteration processes along the Siccar Point group unconformity, Gale crater, Mars: Results from the sample analysis at Mars instrument. *Journal of Geophysical Research: Planets*, 127, e2022JE007387. <https://doi.org/10.1029/2022JE007387>

Received 18 MAY 2022

Accepted 28 OCT 2022







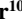







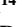
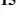



Author Contributions:

Conceptualization: B. Sutter
Formal analysis: B. Sutter
Investigation: B. Sutter
Methodology: B. Sutter, A. C. McAdam

© 2022. The Authors.

This is an open access article under the terms of the [Creative Commons Attribution-NonCommercial-NoDerivs License](#), which permits use and distribution in any medium, provided the original work is properly cited, the use is non-commercial and no modifications or adaptations are made.

Constraining Alteration Processes Along the Siccar Point Group Unconformity, Gale Crater, Mars: Results From the Sample Analysis at Mars Instrument

B. Sutter¹ , A. C. McAdam² , G. M. Wong³, J. V. Clark⁴, P. D. Archer¹, H. B. Franz², P. J. Gasda⁵ , D. W. Ming⁶ , A. Yen⁷ , J. M. T. Lewis^{8,9} , S. P. Schwenzer¹⁰ , S. M. R. Turner¹⁰ , E. B. Rampe⁶ , J. L. Eigenbrode² , J. C. Stern² , L. M. Thompson¹¹ , E. Dehouck¹² , C. Bedford^{6,13} , S. Banham¹⁴ , A. B. Bryk¹⁵ , C. O'Connell-Cooper¹¹ , C. S. House³ , M. Millan^{2,16}, C. Freissinet¹⁷, R. Navarro-Gonzalez^{18,†}, P. R. Mahaffy² , and C. A. Malespin²

¹Jacobs Technology, NASA Johnson Space Center, Houston, TX, USA, ²NASA Goddard Space Flight Center, Greenbelt, MD, USA, ³Department of Geosciences, The Pennsylvania State University, University Park, PA, USA, ⁴GeoControls Systems – JETS Contract, NASA Johnson Space Center, Houston, TX, USA, ⁵Los Alamos National Laboratory, Los Alamos, NM, USA, ⁶NASA Johnson Space Center, Houston, TX, USA, ⁷Jet Propulsion Laboratory, California Institute of Technology, Pasadena, CA, USA, ⁸Department of Physics and Astronomy, Howard University, Washington, DC, USA, ⁹Center for Research and Exploration in Space Science and Technology, NASA GSFC, Greenbelt, MD, USA, ¹⁰Astrobiology OU, School of Environment, Earth and Ecosystem Sciences, The Open University, Milton Keynes, UK, ¹¹Planetary and Space Science Centre, University of New Brunswick, Fredericton, NB, Canada, ¹²Univ Lyon, UCBL, ENSL, UJM, CNRS, LGL-TPE, Villeurbanne, France, ¹³Lunar and Planetary Institute, Universities Space Research Association, Houston, TX, USA, ¹⁴Department of Earth Sciences and Engineering, Imperial College London, London, UK, ¹⁵Earth and Planetary Science, University of California, Berkeley, Berkeley, CA, USA, ¹⁶Department of Biology, Georgetown University, Washington, DC, USA, ¹⁷Laboratoire Atmosphère, Observations Spatiales (LATMOS), LATMOS/IPSL, UVSQ Université Paris-Saclay, Sorbonne Université, CNRS, Guyancourt, France, ¹⁸Instituto de Ciencias Nucleares, Universidad Nacional Autónoma, Ciudad Universitaria, Mexico City, Mexico

Abstract Results from the Sample Analysis at Mars-evolved gas analyzer on board the Mars Science Laboratory *Curiosity* rover constrained the alteration history and habitability potential of rocks sampled across the Siccar Point unconformity in Gale crater. The Glasgow member (Gm) mudstone just below the unconformity had evidence of acid sulfate or Si-poor brine alteration of Fe-smectite to Fe amorphous phases, leaching loss of Fe-Mg-sulfate and exchange of unfractionated sulfur ³⁴S ($\delta^{34}\text{S} = 2\% \pm 7\%$) with enriched ³⁴S ($20\% \pm 5\%$, Vienna Cañon Diablo Troilite). Carbon abundances did not significantly change (322–661 $\mu\text{gC/g}$) consistent with carbon stabilization by amorphous Al- and Fe-hydroxide phases. The Gm mudstone had no detectable oxychlorine and extremely low nitrate. Nitrate (0.06 wt.% NO_3), oxychlorine (0.13 wt.% ClO_4), high C (1,472 $\mu\text{g C/g}$), and low Fe/Mg-sulfate concentration (0.24 wt.% SO_3) depleted in ³⁴S ($\delta^{34}\text{S} = -27\% \pm 7$), were detected in the Stimson formation (Sf) eolian sandstone above the unconformity. Redox disequilibrium through the detections of iron sulfide and sulfate supported limited aqueous processes in the Sf sandstone. Si-poor brines or acidic fluids altered the Gm mudstone just below the unconformity but did not alter underlying Gm mudstones further from the contact. Chemical differences between the Sf and Gm rocks suggested that fluid interaction was minimal between the Sf and Gm rocks. These results suggested that the Gm rocks were altered by subsurface fluids after the Sf placement. Aqueous processes along the unconformity could have provided habitable conditions and in some cases, C and N levels could have supported heterotrophic microbial populations.

Plain Language Summary The Curiosity Rover investigated the chemistry and mineralogy of rocks in the Glen Torridon region of Gale crater, Mars. Rocks sampled across an unconformity (representative of a time gap between when two sedimentary rocks were deposited) gave insight into how they were altered over time. The Glasgow mudstones, below the unconformity, were formed in a lake environment while the younger Stimson sandstones above the unconformity were formed from ancient sand dunes. Using the Sample Analysis at Mars Evolved Gas Analysis (SAM-EGA) experiment, solid powdered samples from these rocks were heated and released gases (e.g., water, carbon dioxide, and sulfur dioxide) were tracked. These gases revealed a complex history of alteration through the rocks. The Glasgow mudstones were characterized by acidic or Si-poor brine alteration, variable sulfur, low amounts of carbon, and no nitrate or oxychlorine.

Writing – original draft: B. Sutter
Writing – review & editing: B. Sutter,
A. C. McAdam

SAM-EGA results from the Stimson sandstone showed rocks that were less altered, had higher levels of carbon, different sulfur compounds and sources, and some nitrate/oxychlorine. Together, these results suggested that the Glasgow rocks were altered by subsurface fluids after Stimson sandstone placement. Aqueous processes along the unconformity could have provided habitable conditions and in some cases, C and N levels could have supported heterotrophic microbial populations.

1. Introduction

A driving factor for sending the Mars Science Laboratory, *Curiosity* rover to Gale crater was the orbital detection of clay minerals in the Glen Torridon (GT) trough suggesting a past aqueous environment that was potentially habitable and thus may contain organic evidence of past microbiology (e.g., Anderson & Bell, 2010; Bennett et al., 2022; Milliken et al., 2010) (Figure 1). Many of the rocks studied by *Curiosity* were deposited in lacustrine and fluvial environments that may have been habitable, and an abundance of diagenetic features suggests a long post-depositional history of groundwater in Gale crater (e.g., Achilles et al., 2020; Frydenvang et al., 2017; Grotzinger et al., 2014, 2015; Nachon et al., 2017; Rampe et al., 2020; Yen et al., 2021). The goal of the Sample Analysis at Mars (SAM) instrument suite onboard *Curiosity* is to evaluate the habitability potential of the Martian surface by assessing the carbon inventory and the chemical and isotopic states of volatile-bearing phases in Gale crater rock, sediment, and soil (Mahaffy et al., 2012). Evaluation of SAM data have indicated a habitable environment with variable redox chemistry may have existed in the GT trough region (House et al., 2022; McAdam et al., 2022; Millan et al., 2022; Williams et al., 2021; Wong et al., 2022). The focus of this work was to evaluate and compare samples collected just above and below the Siccar Point group (SPg) unconformity contact between the GT trough and Greenheugh pediment (Gp) capping unit.

Orbital imaging of the GT trough revealed that Glasgow member (Gm) mudstone immediately below Gp capping unit contact was brighter than stratigraphically lower Gm material, suggesting enhanced aqueous alteration below and close to the contact (Figure 1b). Enhanced aqueous processing along this contact could have implications for preservation of biogenic organic C and was one of the reasons for diverting the MSL rover from the initially planned Mount Sharp Ascent Route to investigate these materials.

Several hypotheses regarding the origin of the bright toned Gm mudstone below the Gp capping unit are possible and include: (a) diagenetic alteration caused by fluids either from upwelling groundwaters or fluids from some other source moving along the contact similar to proposed contact alteration in the Emerson and Naukluft plateau regions and Vera Rubin ridge (VRR; Achilles et al., 2020; Dehouck et al., 2022; Fraeman et al., 2020; Frydenvang et al., 2017; Horgan et al., 2020; Rampe et al., 2017, 2020; Thompson et al., 2022; Yen et al., 2021), (b) downward fluid percolation through the pediment capping unit and into the Gm mudstone just below the contact (Rudolph et al., 2022), (c) subaerial alteration of the mudstone before pediment capping unit deposition (Rudolph et al., 2022), or (d) deposition of the mudstone layer with mineralogy and chemistry that differed from mudstones lower in the same stratigraphic member.

The goal of this work was to utilize the SAM-evolved gas analyzer (EGA) data to constrain the origin of the bright-toned Gm mudstone below the Gp capping unit. SAM data are critical to constraining geologic history and habitability because SAM can detect volatile phases in abundances below the Chemistry Mineralogy (CheMin) X-ray diffractometer detection limit of ~1 wt.%. The SAM instrument is also the only instrument that can detect organic C and, thus, the building blocks of life, and can characterize the composition of the pervasive X-ray amorphous materials in Gale crater. The objectives of this work were to (a) utilize the SAM-EGA results to evaluate the geochemistry and mineralogy of samples just above and below the SPg unconformity, (b) incorporate SAM-EGA data with other results from *Curiosity* to determine the most likely scenario for the formation of the bright toned Gm mudstone below the Gp capping unit, and (c) discuss the implications for microbial habitability in Gale crater relative to the mineralogy/geochemistry detected by the SAM-EGA.

2. Geological Context

2.1. Siccar Point Group Unconformity

The SPg unconformity examined in the GT region occurs between the Gm finely laminated lacustrine mudstone of the Carolyn Shoemaker formation (CSf) and the overlying Gp capping unit of the Stimson formation (Sf)

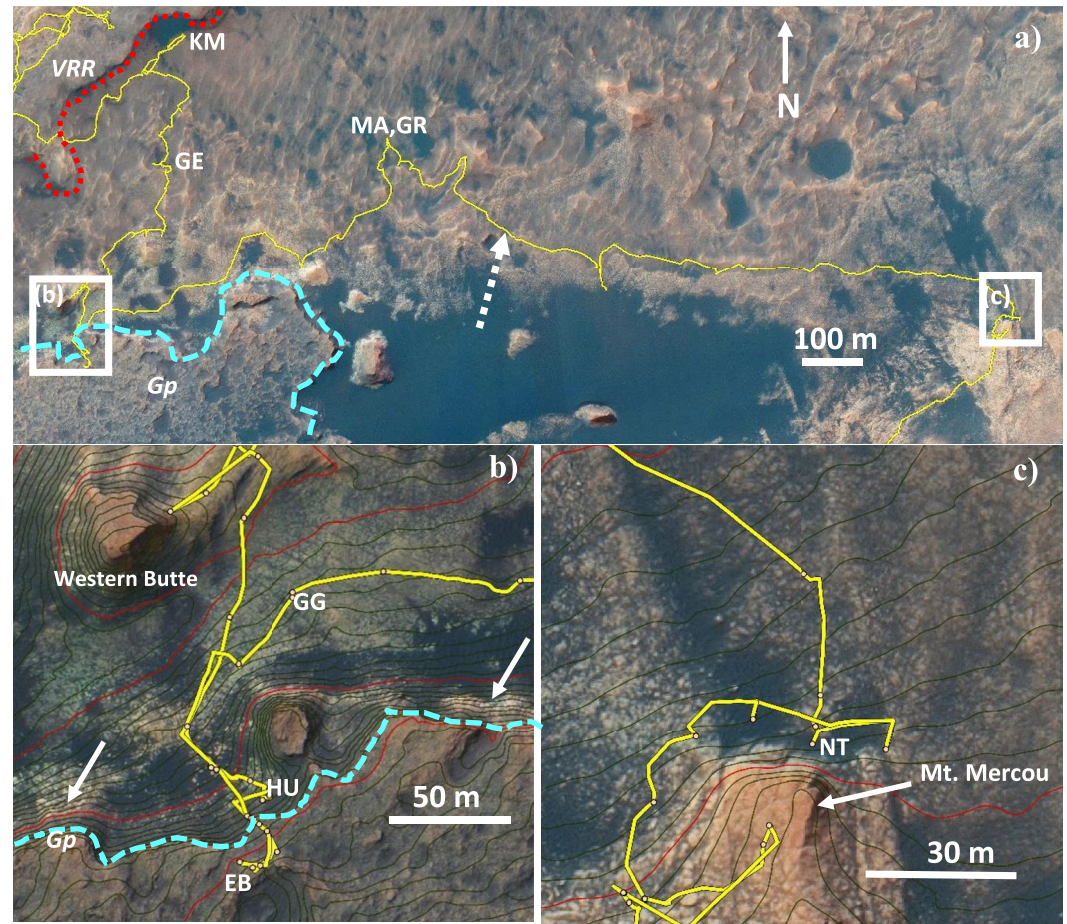


Figure 1. (a) The Glen Torridon (GT) trough between the Greenheugh pediment (Gp) capping unit (south of blue dashed line) and Vera Rubin ridge (VRR) (north of red dotted line). Squares (b and c) refer to panels (b and c), respectively. Yellow lines represent the rover route. The dashed arrow indicates approximate location where the rover encountered the Glasgow member (Gm) material at similar elevation as the Hutton (HU) sample. The stratigraphically lower GT sample locations discussed by McAdam et al. (2022) are indicated: Kilmarie, (KM), Glen Etive (GE), Mary Anning (MA), and Groken (GR). (b) The Glasgow (GG), HU, and Edinburgh (EB) drill sites examined in this work. 1 m contour lines are black and 10 m contour lines are red. Elevation order is $GG < HU < EB$. Blue dashed line marks the Siccar Point unconformity position between the Gp and the underlying Gm mudstone. White arrows indicate bright-toned areas suspected of enhanced aqueous alteration. (c) The Nontron (NT) drill site that occurs under the conformably overlying Mercou member (Mm) sandstone. See Table S1 in Supporting Information S2 for additional sample information and acronym identification. Image Credit: HiRIse, NASA/JPL/University of Arizona.

olian sandstone (Figures 2 and 3, Table S1 in Supporting Information S2). The CSf comprises primarily of fluvial and lake margin deposits of the Knockfarril Hill member, lacustrine deposits of the Gm, fluvial deposits of the Mercou member (Mm), and sedimentary rocks with a strong diagenetic overprint such that depositional environment is indeterminate of the Pontours member (Figure 2) (Fedó et al., 2022). After the erosion of the Gm and stratigraphically higher sediments, eolian sand was deposited over the Gm mudstones and was later buried and cemented resulting in formation of the Sf sandstone (Figure 2) (Banham et al., 2022; Bedford et al., 2022). The Sf sandstone subsequently underwent erosion resulting in the formation of the Gp capping unit. Scarp retreat of the Gp capping unit led to the exposure and then erosion of the broader GT trough including the Gm mudstone (Fedó et al., 2022).

2.2. Carolyn Shoemaker Formation, Glasgow Member Mudstone, and Mercou Member Sandstone

The Gm drilled samples examined by SAM and the CheMin instruments in stratigraphic order (bottom to top) were the Glasgow (GG), Hutton (HU), and Nontron (NT) samples (Figure 2, Figure S1 in Supporting Information S1).

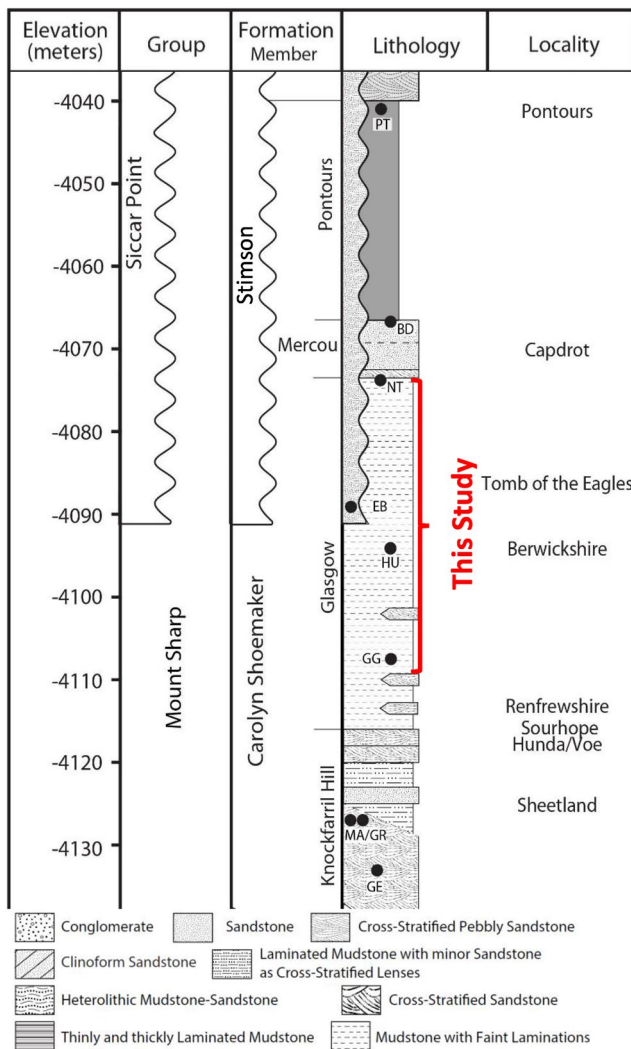


Figure 2. Stratigraphic column providing context for samples examined in this study that occur in the Glasgow member (Gm) of the Carolyn Shoemaker formation (CSf) and one sample in the Stimson formation (Sf). Samples examined in this study are the Glasgow (GG), Hutton (HU), and Nontron (NT), and the Edinburgh (EB) samples. See Table S1 in Supporting Information S2 for additional sample information and acronym identification. The stratigraphic column was adapted from Fedo et al. (2022).

The HU sample occurred in the proposed alteration zone ~1.7 m stratigraphically below the Gp capping unit (Figure 3 and Figure S1c in Supporting Information S1) while the less altered GG and NT samples were 100 m north and ~1.9 km east of HU, respectively (Figures 1 and 3). The GG material was ~14 m stratigraphically below the capping unit. The NT sample resided 22.5 m stratigraphically above HU and just below the conformable contact between the Gm and Mm sandstone (Figures 1 and 2 and Figure S1b in Supporting Information S1). The Mm sandstone had evidence of a fluvial origin and was therefore assigned to the CSf and not to the Sf eolian sandstone that comprises the Gp capping unit (Figure 2).

The Gm mudstone consists of geochemically diverse fractured bedrock (Figure 3, Figures S1 and S2 in Supporting Information S1). The HU sample locality just below the Gp capping unit had distinct geochemical differences relative to the Gm materials (e.g., GG and NT) that occur stratigraphically lower and further from the Gp capping unit. The rover's Alpha Particle X-ray Spectrometer (APXS; Table S2 in Supporting Information S2) and Chemistry and Camera (ChemCam) laser-induced breakdown spectrometer instruments also analyzed the drilled material examined by SAM as well as other bedrock targets close to and related to the drilled samples. Relative to the GG/NT-type samples, gains in Mg, Na, Fe, Ca, and Mn, and lower S and Ni concentrations were detected by the APXS instrument in the HU sampling area and in Gm material just below the nearby (~150 m) capping unit on Western Butte (Figure 1b) (O'Connell-Cooper et al., 2022; Thompson et al., 2022). This indicated the HU-type chemistry was laterally extensive (O'Connell-Cooper et al., 2022; Thompson et al., 2022). ChemCam bedrock analyses detected higher Ca and Na and lower Si abundances in HU-type samples relative to the GG/NT-type samples (Dehouck et al., 2022). Sodium and potassium were found to be correlated in the GG/NT-type samples but not the HU-type samples. Furthermore, chemical index of alteration (CIA) values calculated from ChemCam measurements were ~44 for the HU-type samples compared to ~55 in GG/NT-type samples. The CIA reduction in the HU-type materials was attributed to cation additions (e.g., Ca²⁺, Na⁺, and Mg²⁺) from post-depositional fluids (Dehouck et al., 2022) rather than a lower degree of alteration because secondary mineralogy in HU was distinct from less altered materials in Gale crater (e.g., soil) with similar CIA values as HU. Thus "lower" Si abundances were attributed to dilution through cation addition as opposed to loss through alteration (Dehouck et al., 2022; Thompson et al., 2022). ChemCam detected elevated F levels in the HU-type bedrock that were correlated with Ca and sometimes P (Forni et al., 2020, 2021) consistent with fluorapatite (Thorpe et al., 2022).

Post-depositional alteration of the HU-type materials rather than sediment source differences were likely responsible for the geochemical differences between HU-type and GG/NT-type materials (Dehouck et al., 2022; Thompson et al., 2022). HU-type chemistry was detected only at locations close to the unconformity in the HU sampling area and the highest Gm point the rover accessed just below the Gp capping unit on Western Butte (Figure 1b). Similar chemistry to HU was not reported by APXS and ChemCam at stratigraphically equivalent elevations (~-4,095.7 m) further along the traverse (Figure 1a, dashed arrow) (Dehouck et al., 2022; O'Connell-Cooper et al., 2022; Thompson et al., 2022). The APXS and ChemCam derived geochemistry of these stratigraphically equivalent HU sediment layers are similar to GG/NT-type samples, which suggested these materials existed at deeper depths and were out of reach of alteration processes that occurred along the contact.

The Gm mudstones were characterized by nodules and calcium sulfate veins (Figure 4). The nodules could be related to post-depositional diagenetic processes or formed soon after deposition but before lithification as the nodules did not appear to disrupt the bedrock fabric (Gasda et al., 2022; Rudolph et al., 2022). The

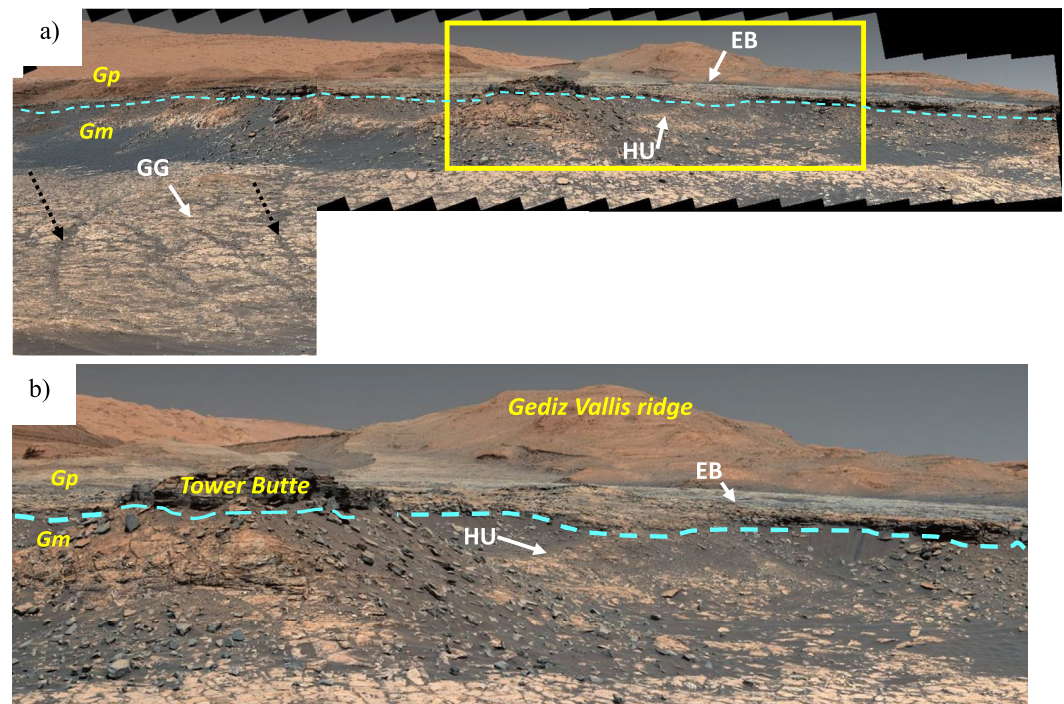


Figure 3. (a) Context image for samples along the Siccar Point unconformity (blue dashed line). Glasgow member (Gm) mudstone samples: Glasgow (GG), and Hutton (HU). Greenheugh pediment (Gp) sample: Edinburgh (EB). Elevation difference between GG and EB is ~ 20 m. Note sand filled fracturing examples in Gm sediments indicated by dotted black arrows (Mastcam MR_mcam13827, 13796). (b) Closer view (yellow rectangle panel (a)) of the Siccar Point unconformity contact (blue dashed line) between the Gp and the underlying Gm mudstones. Both images look south toward Gediz Vallis Ridge. (Mastcam MR_mcam13796, 13827). Image credit NASA/JPL-Caltech/Malin Space Science Systems.

nodule chemistry was Fe, Mg, or Mn rich and in many cases did not differ from the nodule-free bedrock (Gasda et al., 2022; Thompson et al., 2022). Cross-cutting Ca-sulfate veins were present throughout all Gm mudstones indicating a post-depositional process that added Ca-sulfate after sediment lithification (Figure 4 and Figure S1a in Supporting Information S1).

The HU-type material (including samples below Gp capping unit on Western Butte) was crosscut by dark-toned Fe and Mn enriched veins and associated light-toned, resistant features rich in Mg, K, and F (Gasda et al., 2022; Thompson et al., 2022) (Figure S2 in Supporting Information S1). These veins and linear features were only detected in HU-type material. The cross-cutting nature of the veins suggested that fluids responsible for vein forming occurred after lithification.

The mineralogy of HU was distinctly different from the GG and NT samples. The HU mineralogy had relatively higher cristobalite, magnetite, apatite, and pyroxene and lacked anhydrite and had lower hematite and clay content than the GG and NT samples (Table S3 in Supporting Information S2) (Thorpe et al., 2022). Mastcam visible near infrared (VNIR) analyses, furthermore, revealed spectral differences between the GG and HU materials (Rudolph et al., 2022). The GG material had red slope up to <640 with weak absorption at 867 nm consistent with fine-grained red hematite while the mostly flat VNIR HU spectra were consistent with coarse grained hematite. This coarse-grained hematite in HU was proposed to have formed as result of late-diagenetic process that transformed the earlier formed fine-grained hematite to coarse-grained hematite (Horgan et al., 2020; Rudolph et al., 2022). However, the high magnetite (6.2 wt.%) in HU, which was not detected in GG, suggested that the HU magnetite instead of hematite (which is low 2.4 wt.%) (Table S3 in Supporting Information S2) could be the source of the mostly flat VNIR HU spectra (Rudolph et al., 2022).

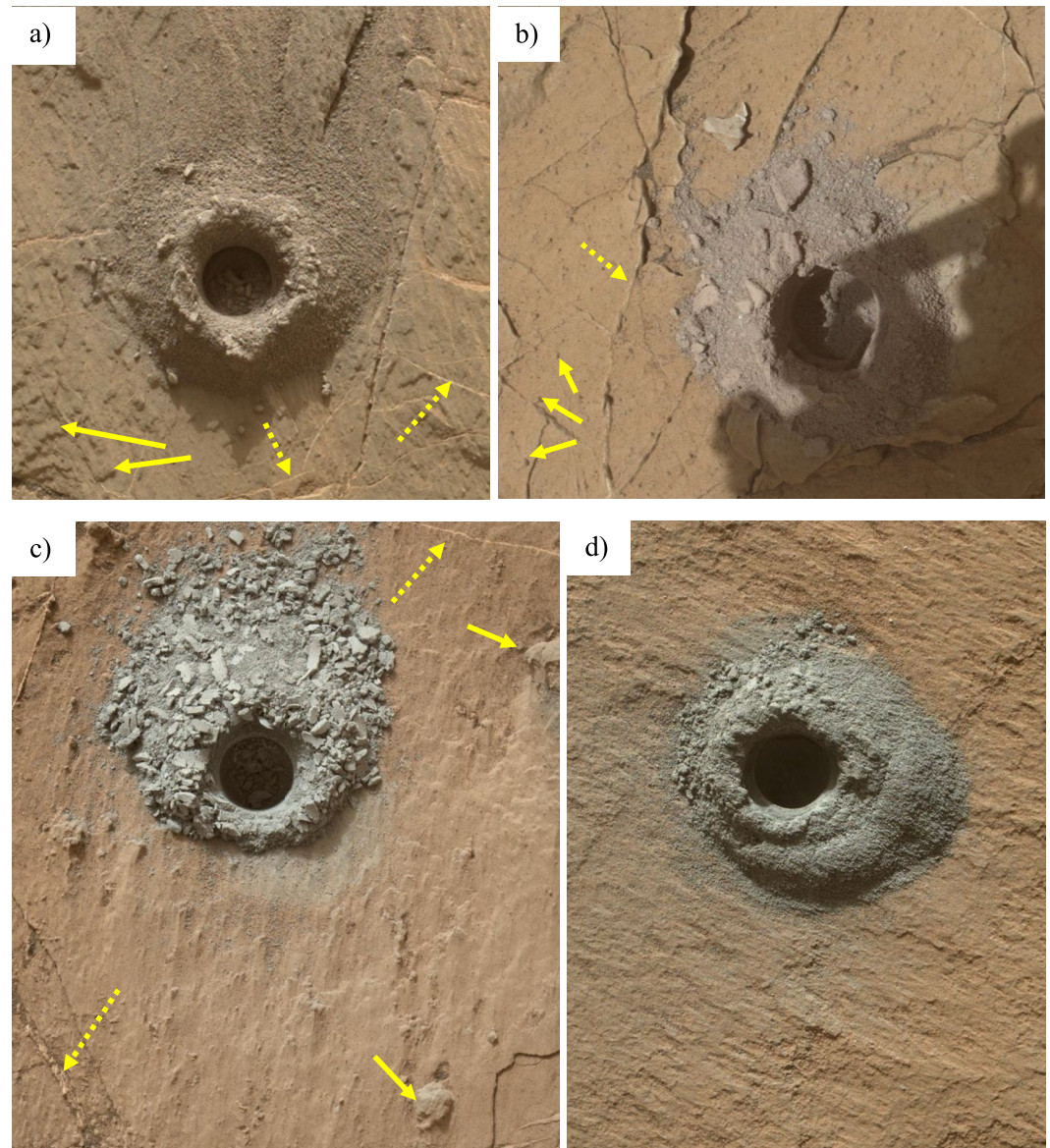


Figure 4. Drill hole MAHLI images for (a) Glasgow (GG), (b) Nontron (NT), (c) Hutton (HU), and (d) Edinburgh (EB). Solid arrows refer to concretions/nodules while dashed lines point to Ca-sulfate veins in the GG, NT, and HU samples. Drill hole diameter 1.6 cm. GG (2773MH0004240011002826C00), NT (3068MH0006190011101166C00), HU (2684MH0001970011001666C00), and EB (2724MH0001970011002432C00). Image credit NASA/JPL-Caltech/MSSS.

2.3. Siccar Point Group, Stimson Formation, and Greenheugh Pediment

The Edinburgh (EB) sample examined by SAM was drilled within the Gp capping unit (Figures 1a and 1b), which was a continuation of Sf sandstone that occurred at lower elevations (e.g., Emerson and Naukluft plateaus, and Murray buttes) (Banham et al., 2018, 2021, 2022; Bedford et al., 2020, 2022). The Gp capping unit consisted of three stratigraphic intervals; the Gleann Beag interval (1–3.6 m thick), Ladder interval (~1.3 m), and EB interval (~1.5 m). The intervals reflect differences in depositional wind directions which were, north-northeast, south, and west for the Gleann Beag, Ladder, and EB intervals, respectively (Banham et al., 2022). The Gleann Beag depositional direction and geochemistry was similar to lower Sf materials (Murray buttes and Emerson plateau) suggesting Gleann Beag shared a similar provenance as the lower Sf sandstones (Banham et al., 2022; Bedford et al., 2022; Thompson et al., 2022). In contrast, the Ladder and EB intervals were characterized by more than

twice the K concentration of the Gleann Beag and lower Sf sandstones, as well as trending to higher Na, Fe, and Cr, and lower Ti, P, and Ni concentrations (Thompson et al., 2022).

The EB drill site in the EB interval consisted of fractured bedrock that was infilled with eolian fines (Figure S3 in Supporting Information S1). Unlike the Emerson and Naukluft plateau materials that had Si and S enriched alteration halos (Yen et al., 2017), no alteration halos were observed around EB nor throughout the Gp capping unit or in any of the intervals below EB. Concretions while present in the lower Gleann Beag interval, were rare in the EB interval materials and were not present at the EB drill site (Figure 4d) (Banham et al., 2022; Bedford et al., 2022).

The EB sandstone mineralogy was mostly similar to previously investigated Big Sky (BS) Sf sandstone but there were notable differences. Olivine and a phyllosilicate were detected in EB but not BS and EB had twice as much K-feldspar than BS (Thorpe et al., 2022; Yen et al., 2017). The presence of olivine in EB was consistent with less post-depositional alteration in EB than BS or that the EB sandstone was derived from a source with more olivine than the BS sandstone (Bedford et al., 2022). The high-energy environment conducive to eolian sand dune deposition suggested that finer grained material containing the EB smectite was not detrital (e.g., McKinley et al., 2003). Furthermore, the absence of phyllosilicates in modern Martian eolian sediments (Rampe et al., 2018) suggested that detrital phyllosilicate deposition was unlikely in the EB sandstone. While detrital phyllosilicate cannot be ruled out completely, the EB phyllosilicate was likely derived from sandstone alteration after deposition (Bedford et al., 2022). The low concentration of the phyllosilicate (Table S3 in Supporting Information S2) prevented identification of the type of phyllosilicate by CheMin; however, evolved water detections from SAM analyses were consistent with the presence of nontronite and montmorillonite (discussed below).

3. Materials and Methods

3.1. Drilled Samples

The samples analyzed in this work include the GG (−4,107.8 m), NT (−4,072.9), and HU (−4,095.4 m) samples from the Gm mudstone in addition to the EB (−4,088.7 m) Gp capping unit sandstone sample (Figure 4). The GG and NT geochemical and mineralogical differences discussed above relative to the HU sample suggested the GG and NT materials were less altered than HU and were not exposed to the proposed alteration processes that affected HU. The more altered HU material will be compared to the related but less altered GG and NT materials to determine the nature of the alterations scenario(s) that affected HU. Examination of the EB sample is anticipated to determine if Gp capping unit fluids that may have contributed to altering HU.

3.2. SAM Instrument

The SAM instrument suit is composed of three instruments that analyze evolved gases from Gale crater sediments: the quadrupole mass spectrometer (QMS), the gas chromatography columns (gas chromatography mass spectrometry [GCMS]), and the tunable laser spectrometer (TLS) (Mahaffy et al., 2012). Before sample acquisition, the selected SAM quartz sample cup was preconditioned at 900°C (5 min) while gas transfer lines and manifolds were preconditioned to 135°C to minimize background contributions during SAM analysis. A drilled sample was subsequently delivered to the SAM quartz cup and then sealed into one of the two SAM ovens. The difference between the two ovens was that Oven 1 heated samples to ~860°C (GG, NT, and EB samples) while Oven 2 (HU sample) had an auxiliary heater that permitted heating samples to 890°C (Mahaffy et al., 2012). Oven choice was usually the result of ensuring that both ovens were evenly used to avoid extra wear on one oven over the other. The SAM oven was heated (~35°C min^{−1}) while He carrier gas (~0.8 sccm; 25 mbar) swept evolved gases to the QMS for identification. This analysis was termed SAM-EGA mode where evolved gases (e.g., H₂O, SO₂, CO₂, CO, O₂, NO, and HCl) released at characteristic temperatures from volatile bearing phases were used to identify mineral and/or organic phases. Evolved gases were delivered directly to the QMS while portions of the gases were delivered to either the TLS or GCMS. The first SAM-EGA analyses always delivered evolved gas to both the QMS and TLS. Sometimes a second sample analysis was requested based on the desire to improve organic C detection, such that evolved gases were sent directly to the QMS for EGA and a portion of the gases were sent to the GCMS for analysis. Most of the samples analyzed in this work resulted in requests for a second analysis by the GCMS and thus a replicate SAM-EGA results for GG, NT, and HU samples were acquired and were termed GG1, GG2, NT1, NT2, HU1, and HU2, respectively. To conserve sample cups, all replicate

analyses were conducted by adding sample over the previous sample in the same cup. No evidence for organics in the EB sample was present; thus, only one SAM-EGA with TLS analysis was conducted. All GCMS analyses and associated hydrocarbon detections were discussed by Millan et al. (2022). Some TLS results regarding CH₄ isotopes were evaluated by House et al. (2022). Evolved gases analyzed and discussed in this work include H₂O (m/z 17), SO₂ (m/z 64), CO₂ (m/z 44), CO (m/z 28), O₂ (m/z 32), NO (m/z 30), HCl (m/z 36), H₂ (m/z 2), and H₂S (m/z 34). Water identification by m/z 17 was used because m/z 18 was always saturated. Procedures for deriving reported δ³⁴S values from evolved SO₂ detections can be found in Franz et al. (2017) and Wong et al. (2022).

3.3. Evolved Gas Corrections

Evolved gas detections in some cases, require corrections to account for contributing fragments of the same mass from other evolved gases. Preflight analyses of calcite and melanterite provided isotopologue corrections for CO and H₂S, respectively. Other corrections were derived from SAM-EGA analyses. Isotopologue correction factors for CO (m/z 28) and NO (m/z 30) were also obtained from NIST mass spectrum analyses of gas species that resides in the NIST Standard Reference Database (NIST-SRD, 2021).

O₂ required corrections attributed to contributions from H₂O and sulfate decomposition. Except for the EB sample, O₂ fragments from H₂O fragmentation and sulfate decomposition were the main contributors to the m/z 32 signal in all samples discussed in this work. This was because the low intensity m/z 32 signal followed the m/z 17 and m/z 64 signals extremely well at temperatures that were not typical of O₂ producing phases like perchlorate or chlorate (here after referred to as oxychlorine when presence of both phases is possible). The m/z 32/m/z 17 and m/z 32/m/z 64 ratios used for removing O₂ contributions from H₂O and SO₂ were acquired at temperatures where thermal decomposition of oxychlorine phases did not occur.

$$O_2 = m/z\ 32 - 0.043 \times m/z\ 64 - 0.074 \times m/z\ 17$$

The derivatization agents, N-methyl-N-(tert-butyl-dimethylsilyl) trifluoroacetamide (MTBSTFA) and dimethyl-formamide (DMF), used for wet chemistry SAM-GCMS analysis leaked from at least one of the sealed wet chemistry cups (Freissinet et al., 2015; Glavin et al., 2013). The MTBSTFA/DMF decomposition byproducts had isotopologue contributions that required correcting from masses of interest. The m/z 30 attributed to NO from nitrate decomposition typically had contributions from the MTBSTFA/DMF byproducts formaldehyde and ethane. However, formaldehyde also had contributions from methyl propene (m/z 39) and ethane (m/z 25) that required correcting first. Methanol (m/z 31) corrections were applied to the NT samples only (*italics below*)[†] because methanol contributions to the SAM background occurred after the tetramethylammonium hydroxide (TMAH) derivatization analysis of the Mary Anning 3 (MA3) sample (Williams et al., 2021). The TMAH analysis of MA3 occurred after the GG, HU, and EB analyses but before the NT analyses.

$$\text{Formaldehyde} = m/z\ 29 - 0.24 \times m/z\ 39 - 6.15 \times m/z\ 25 - [0.46 \times m/z\ 31]^\dagger$$

$$\text{Nitrate} - \text{NO} = m/z\ 30 - 0.8 \times \text{Formaldehyde} - 7.18 \times m/z\ 25 - [0.0649 \times m/z\ 31]^\dagger$$

CO (m/z 28) had the most corrections due to contributions from MTBSTFA by-products such as methyl propene (m/z 39), formaldehyde (m/z 29), and ethane (m/z 25), and CO₂ (m/z 45). The same formaldehyde correction was used for m/z 29 as in the correction for evolved NO (m/z 30).

$$CO = m/z\ 28 - 3.2 \times m/z\ 45 - 0.49 \times m/z\ 39 - 0.24 \times \text{Formaldehyde} - 28.6 \times m/z\ 25 - [0.05 \times m/z\ 31]^\dagger$$

Total evolved gas releases (e.g., μmol or nmol) were quantified using the procedures described elsewhere (Archer et al., 2014). Evolved gas totals were combined with estimated sample mass delivery to the SAM quartz cup to calculate evolved gas contents (e.g., wt.% or μg/g). Evolved gas content errors were based on propagation of errors derived from sample mass delivery and evolved gas totals.

3.4. SAM Sample Delivery Determination

Estimated sample mass delivery of a single drilled portion to SAM (45 ± 18 mg) was originally based on work with MSL testbed hardware and was applied to all drilled samples before and including the Quela sample. However, the drill feed mechanism began to fail on sol 1536, which resulted in the development of the Feed

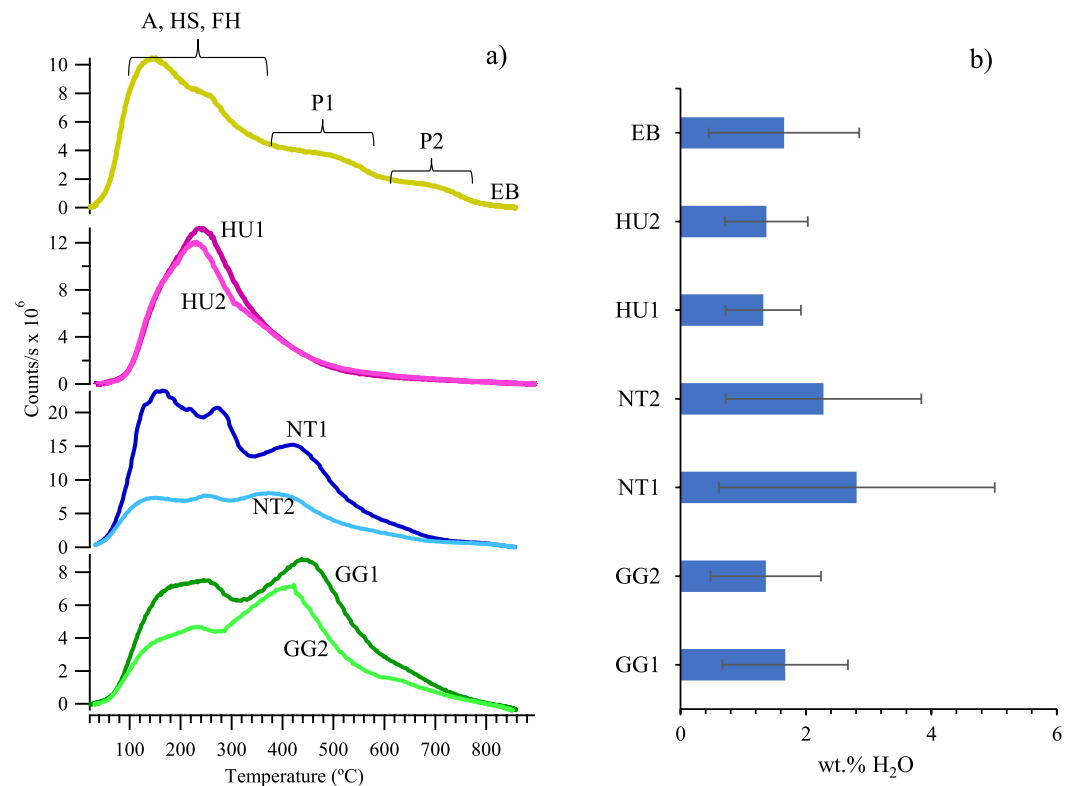


Figure 5. (a) Evolved water (m/z 17) versus temperature. (b) Water concentration for the Glasgow (GG), Nontron (NT), Hutton (HU), and Edinburgh (EB) samples. Temperature ranges for evolved H₂O sources indicated in brackets. Adsorbed water (a), hydrated salts (HS), poorly crystalline Fe-(oxy)hydroxides (FHs) and, phyllosilicate hydroxyls (P1 and P2).

Extended Drilling technique that used the rover arm to extend and retract the drill into the target rock. The feed-extended sample transfer (FEST) procedure then deposited the drilled sample into SAM by placing the drill over the SAM inlet reversing the drill to permit the fines to fall into the SAM sample cup (Fraeman et al., 2020; McAdam et al., 2020). The FEST procedure bypassed the portioning and sieving (<150 μm) capability of Collection and Handling for Interior Martian Rock Analysis tool which prevented knowing how much sample was being delivered to SAM. Sample mass delivery to SAM was estimated by utilizing water bearing phase (e.g., gypsum, bassanite, and smectite) weight percentages determined by CheMin in conjunction with total evolved water associated with those phases to calculate how much sample was delivered to SAM (McAdam et al., 2020). This method did not affect the error associated with total evolved gas detected by SAM (e.g., μmol). The greater error associated with estimating sample mass delivery with this technique did result in increased abundance (e.g., wt.%, $\mu\text{g/g}$) errors relative to previous abundance calculations (e.g., Sutter et al., 2017).

4. Results

4.1. H₂O

The GG, NT, HU, and EB samples evolved H₂O (1.3–2.8 wt.% H₂O) with peaks at similar temperatures; however, the relative peak intensities varied between samples (Figure 5, Table S4 in Supporting Information S2). The two peaks below 300°C in all samples were attributed to adsorbed water, hydrated salts (HSs), and/or dehydroxylation of poorly crystalline Fe-(oxy)hydroxides (FH). The first main water peak (~160°C) observed in all samples was consistent with the presence of bassanite ($\text{CaSO}_4 \cdot 0.5\text{H}_2\text{O}$), which was detected by the CheMin instrument in the GG and NT samples (Thorpe et al., 2022). Bassanite was not detected in HU or EB suggesting that the ~160°C water peak either belonged to an amorphous hydrated CaSO_4 or other HS. The NT and GG water peaks below 300°C had similar intensities that differed from HU, which had relatively more intense and broader ~220°C peak

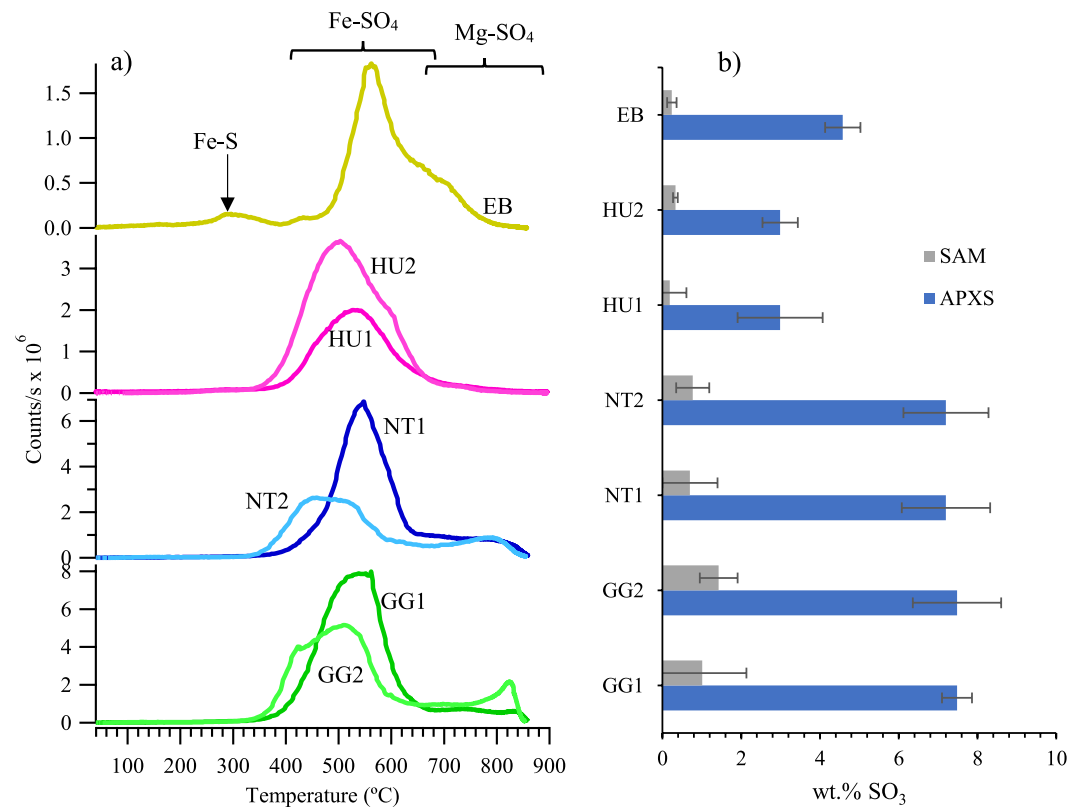


Figure 6. (a) Evolved SO₂ (m/z 64) versus temperature. (b) Sulfur abundance detected by Sample Analysis at Mars (SAM) and the Alpha Particle X-ray Spectrometer (APXS) instrument. Temperature ranges for evolved SO₂ sources indicated in brackets. Iron sulfate (Fe-SO₄), magnesium sulfate (Mg-SO₄), and iron sulfide (Fe-S).

that was consistent with hydrated amorphous Fe-hydroxide phase that is known to evolve water during thermal decomposition near these temperatures (Hogancamp et al., 2018) (Figure 5).

The GG, NT, and EB samples had significant evolved water between 400°C and 500°C while HU had no obvious peak in that temperature range. The evolved water peak indicated by P1 in Figure 5 was consistent with an Fe-smectite (e.g., nontronite) and was consistent with ChemMin detections of Fe-smectite in these samples (Thorpe et al., 2022) (Figure 5). Above 600°C, GG, NT, and EB also had an additional evolved water peak (Peak P2 in Figure 5) that was not detected in HU. This evolved water release was consistent with Al-bearing smectite (e.g., montmorillonite).

4.2. SO₂

The evolved SO₂ release patterns below 675°C in the GG, NT, and HU, samples were consistent with Fe-sulfate bearing phases (Figure 6a) (McAdam et al., 2014). The presence of multiple peaks with varying intensities within each SO₂ evolution suggested the possibility that multiple Fe-sulfate phases were present within each sample. The temperature of the main Fe sulfate peaks for HU2, GG2, and NT2, trended slightly lower than the HU1, GG1, and NT1 samples and this could be attributed to heating and He flow rates differences because of the second sample being placed over the first sample. This phenomenon of replicate peak temperatures being lower than first analysis peak temperatures was also observed with mid-temperature water peaks along with main CO₂ and CO peaks as well (Figures 5a, 7a and 8a).

Evolved SO₂ peaks above 750°C in GG2 and NT2 were consistent with the presence of Mg-sulfate (Figure 6a). GG2 had a pronounced peak at ~821°C while NT2 had broad release that peaked near 780°C. The intensity of evolved SO₂ at these temperatures was much lower in GG1 and NT1 demonstrating the heterogeneity of

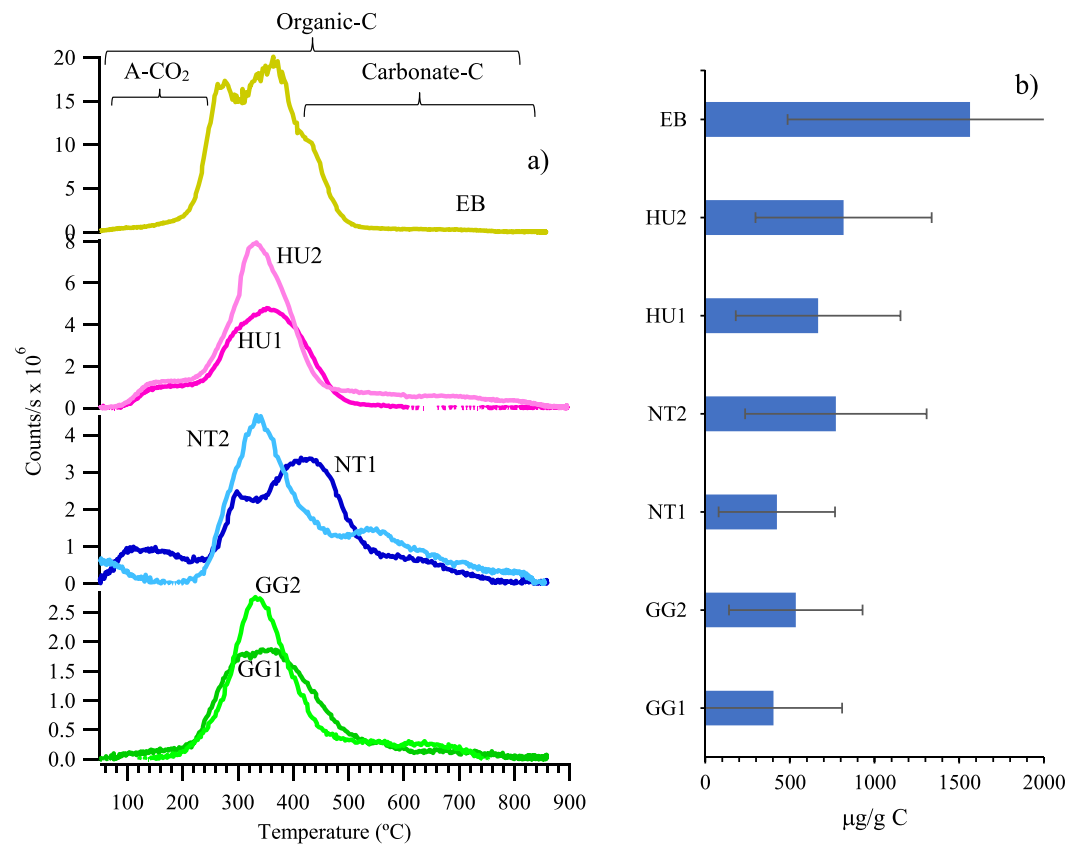


Figure 7. (a) Evolved CO₂ (m/z 44) versus temperature. (b) Total CO₂ concentration reported as total C. Temperature ranges for evolved CO₂ sources indicated in brackets. Atmospherically adsorbed-CO₂ (A-CO₂).

Mg-sulfate occurrence in these samples. No high temperature SO₂ releases consistent with Mg-sulfate were detected in the HU sample.

The SAM and APXS total S abundances were lower in the HU sample versus the GG and NT samples (Figure 6b). The SAM S abundances were also much lower (0.19–1.43 wt.% SO₃) than the total S detected by the APXS (2.99–7.48 wt.%) and ranged from 9% to 16% of total S (Figure 6b; Table S5 in Supporting Information S2). The lower SAM-S detections relative to APXS total S were attributed to the samples having more calcium sulfate than Fe and Mg-sulfate phases as the SAM oven temperature range is too low to thermally decompose calcium sulfate.

The evolved SO₂ release pattern from EB differed from the Gm samples as EB had multiple releases spread over a wider temperature range than the Gm samples. A low intensity SO₂ peak in the EB sample was present at 300°C followed by a main peak at 560°C and lesser peaks at 660°C and 700°C (Figure 6a). The lowest temperature EB SO₂ peak coincided with evolved O₂ derived from oxychlorine decomposition which was consistent with the oxidation of reduced Fe-sulfide by evolved O₂ (Figure S4 in Supporting Information S1) (Wong et al., 2022). The higher temperature peaks at 560°C and 660°C were consistent with Fe-sulfate phases and possibly an Fe-Mg-sulfate phase at 700°C (Franz et al., 2017). The SAM sulfur abundance in EB was only 5.2% of the total S detected by APXS, which also indicated that a small fraction of the total S in the EB sample was derived from Fe- and Mg S-phases (Table S5 in Supporting Information S2).

Isotopic analyses revealed three distinct δ³⁴S values across the SPg unconformity. The δ³⁴S values were relatively unfractionated (−5 to 5 δ³⁴S‰, Vienna Cañon Diablo Troilite), for less altered GG and NT sediments. The more altered HU samples had highly enriched δ³⁴S values (18–21 δ³⁴S‰) while the EB sandstone was characterized by depleted δ³⁴S values (−27 δ³⁴S‰) (Table S5 in Supporting Information S2) (Wong et al., 2022).

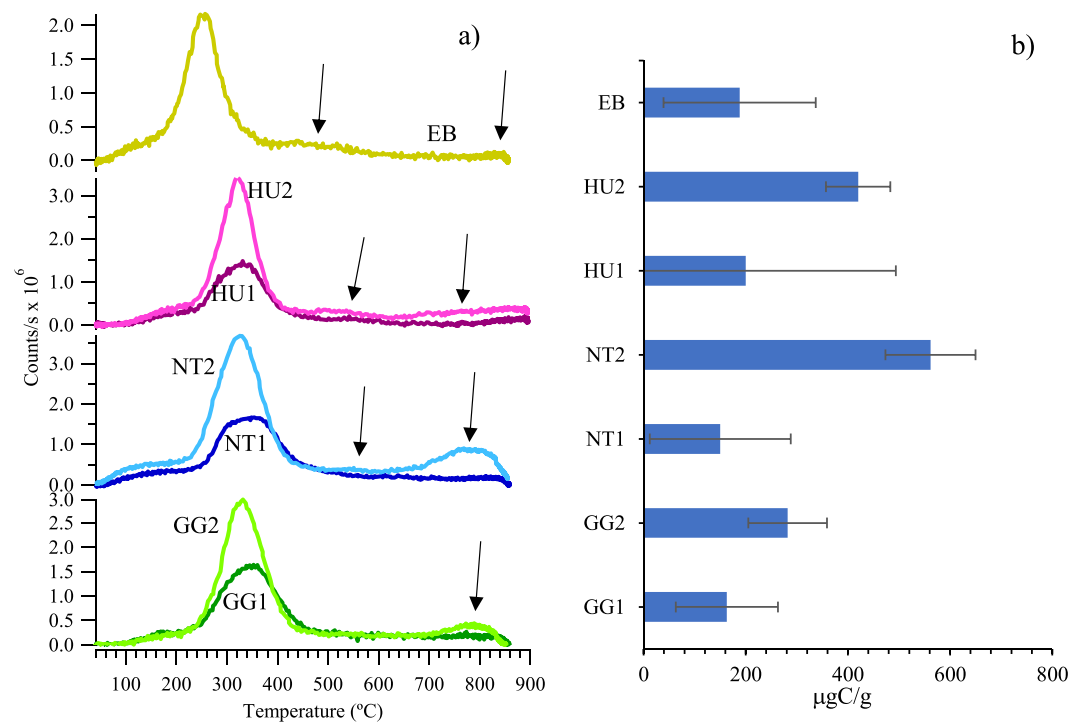


Figure 8. (a) Evolved CO (m/z 28) versus temperature as detected by the Sample Analysis at Mars-evolved gas analyzer. (b) Total C derived from evolved CO detections. Arrows indicate locations of high temperature CO releases of relatively lower intensity described in main text.

4.3. CO₂/CO

Evolved CO₂ from GG1, GG2, NT2, HU1, and HU2 mostly consisted of a major CO₂ release that peaked at a similar temperature (330°C–345°C) (Figure 7a). The NT2 sample had an additional CO₂ peak at 550°C. The evolved CO₂ from NT1 differed from the other Gm samples in having two peaks at ~295°C and 420°C. The Gm C abundances were similar within error and ranged from 302 to 702 µgC/g (Figure 7b, Table S6 in Supporting Information S2). The EB sample had the highest abundance of evolved CO₂ relative to the Gm samples (Table S6 in Supporting Information S2). The CO₂ in EB was characterized by a release pattern with three distinct peaks (270°C, 365°C, and 425°C) that differed from the Gm samples (Figure 7).

Evolved CO was detected in all samples where the most intense CO release for each sample occurred at a similar temperature as the most intense CO₂ release except in EB (Figures 7a and 8a). The EB CO release coincided with the lowest temperature and second most intense CO₂ release. The main CO release for GG, NT and HU samples occurred between 200°C and 450°C while the main EB CO release occurred at lower temperatures between 150°C and 350°C. The abundances of evolved CO were variable and ranged between 163 and 562 µg C/g (Table S7 in Supporting Information S2).

All evolved CO₂ and CO were consistent with the presence of oxidized organic carbon throughout the entire temperature range, though carbonates could also have contributed to evolved CO₂ above 400°C (Figure S5 in Supporting Information S1). Combustion of organic C was possible in EB as evolved O₂ occurred at similar temperature as evolved CO₂ and CO (Figure S6 in Supporting Information S1).

4.3.1. Low Temperature CO₂/CO (<450°C)

The most intense peaks of evolved CO₂ and CO occurred below 450°C (Figures 7a and 8a); however, poor matches to laboratory analog analyses of candidate oxidized organic C phases created challenges in identifying the C source of this low temperature CO₂ and CO. Ionizing radiation that oxidizes organic carbon from meteoritic (e.g., Flynn, 1996) or Martian magmatic sources (Steele et al., 2016, 2018) to yield metastable acetate, oxalate, and benzoate has been proposed to affect the Martian surface down to 1 m depth (Applin et al., 2015; Benner et al., 2000; Eigenbrode et al., 2014; Fox et al., 2019; Freissinet et al., 2020; Lewis et al., 2021; Pavlov

et al., 2012). Evolved CO₂ temperatures from the GG, NT, HU, and EB samples occurred at similar temperatures observed in laboratory analog Fe- and Al-acetate analyses (Clara et al., 2003; Dollimore, 1987; Lewis et al., 2021). However, evolved acetone (m/z 58) or acetic acid (m/z 43) typical of acetate thermal decomposition (Jewur & Kuriacose, 1977; Judd et al., 1974; Lewis et al., 2021) were not detected consistent with the absence of acetate. Evidence of benzoate was also lacking as benzophenone and/or benzoic acid typical of benzoate thermal decomposition were not detected (Abrams et al., 1984; Freissinet et al., 2020; Vlase et al., 2005).

Laboratory analog thermal analyses of a series of oxalates demonstrated that Fe(II)-oxalate coevolved CO and CO₂ at temperatures closest to those observed in the Gm and EB samples (Lewis et al., 2021). Unfortunately, laboratory Fe(II)-oxalates co-evolved CO₂ and CO 75°C–100°C and 150°C, respectively, higher than what was observed in the Gm and EB samples. These laboratory analog analyses of Fe(II)-oxalates mixed with silica may not have accurately captured the mineralogical and chemical environment in Gale crater sediments, thus preventing exact CO₂ and CO matches to the Gm and EB data. Future laboratory studies analyzing oxalate/Mars basaltic analog mixtures could capture the complex oxalate/basaltic chemical interactions during heating that could yield evolved CO₂/CO results consistent with Gm and EB detections.

Decarbonylation and decarboxylation of more complex organic C from meteoritic (e.g., Okumura & Mimura, 2011; Remusat et al., 2005) or magmatic macromolecular C (Steele et al., 2016, 2018) that was partially oxidized by ionizing radiation could have contributed to evolved CO and CO₂ detected below 450°C. The detection (150–300 ppb) of chlorobenzene and lesser amounts of C₂ to C₄ dichloroalkanes in the Gale crater Cumberland sample (Freissinet et al., 2015), suggested that more complex oxidized organics could persist despite the destructive effects of ionizing radiation and thus, contribute to evolved CO₂ and CO detections. Evidence of un-oxidized phases in Gale crater samples was demonstrated by combustion GCMS analysis of the Cumberland mudstone sample that yielded significantly more evolved CO₂ than the non-combusted Cumberland sample (Stern et al., 2022). Results from the combustion analysis demonstrated that complex hydrocarbons containing carbonyl and carboxyl groups may persist in Gale sediments.

Evolved CO₂ and CO in the EB sample below 400°C were consistent with contributions from combustion by evolved O₂ from oxychlorine thermal decomposition (Figure S6 in Supporting Information S1). Evolved O₂ overlapped with evolved CO₂ and CO suggesting that evolved O₂ from oxychlorine decomposition could have contributed to evolved CO₂ and CO. The evolved O₂ peak did not necessarily correspond with all evolved CO₂ and CO peaks suggesting organic C combustion likely did not dominate the evolved CO₂ and CO detections in EB. Nevertheless, combusted organic C at these temperatures would demonstrate the presence of phases that had not been completely oxidized by ionizing radiation similar to what was detected in the Cumberland combustion analyses (Stern et al., 2022). The non-detection of evolved O₂ in the GG, NT, and HU samples suggested that CO₂ and CO combustion products were unlikely in those samples. Limited CO₂ and CO combustion products; however, cannot be excluded from the GG, NT, and HU samples as very low oxychlorine abundances could have evolved O₂ that was completely consumed by combustion.

4.3.2. High Temperature CO₂/CO (>450°C)

Much less intense CO₂ and CO detections above 450°C (Figures 7a, 8a and 9) were consistent with contributions from Na, K, Mg, or Ca oxalates (Dollimore & Griffiths, 1970; Lewis et al., 2021; Mohamed et al., 2002). Above 600°C evolved low intensity CO₂ and CO releases could also have contributions from CO₂ and CO present in glass vesicles (e.g., Macpherson et al., 1999; Pineau & Javoy, 1994). The high concentration of amorphous material in the Gm and EB samples (Table S3 in Supporting Information S2) suggests vesicles if occurring in primary glass phases could contribute evolved CO₂ and CO at these temperatures.

Meteoritic, magmatic macromolecular, or geologically reworked microbial organic C could also have contributed evolved CO₂ and CO above 600°C similar to what has been proposed for other Gale crater sediments (Eigenbrode et al., 2018). Larger macromolecular organic compounds could be more refractory and resist thermal decomposition at lower temperatures and evolve CO₂ and CO through decarboxylation/decarbonylation reactions at higher temperatures.

Evolved CO₂ above 400°C in the GG, NT, HU, and EB samples could have contributions from carbonates (Figure S5 in Supporting Information S1). Evolved CO₂ temperatures demonstrated that NT1 and EB samples had peaks consistent with siderite, while a NT2 peak (~550°C) was consistent with magnesite (Figure S5 in Supporting Information S1). Instead of siderite or magnesite, CheMin detected ankerite [(Ca, Fe)CO₃] (0.9 wt.%) in NT.

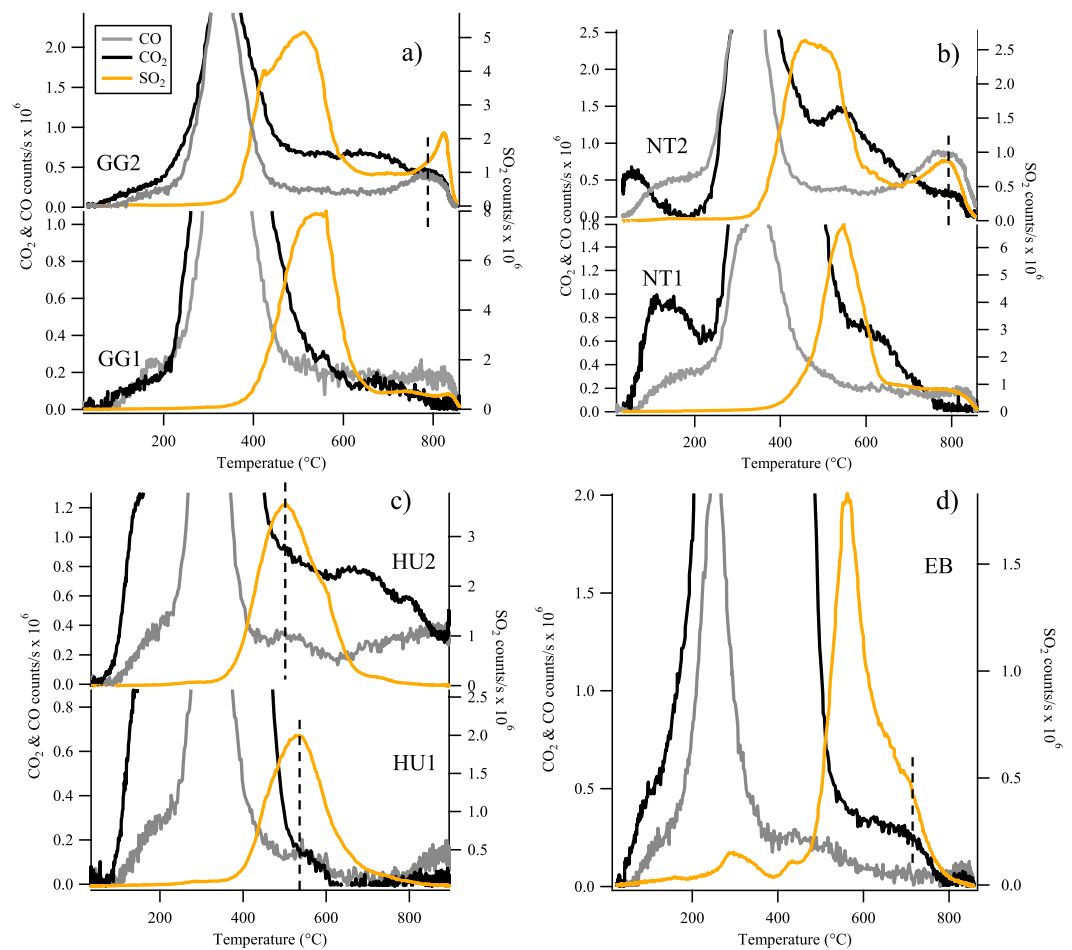


Figure 9. Evolved CO_2 , CO, and SO_2 from (a) Glasgow, (b) Nontron, (c) Hutton, and (d) Edinburgh. Vertical dashed lines indicate temperatures of co-evolution of CO_2 , CO, and SO_2 in the GG2, NT2, HU, and EB samples.

This discrepancy between carbonates possibly detected by SAM (siderite vs. magnesite) and between SAM and CheMin (siderite/magnesite vs. ankerite) demonstrated the heterogeneity that can exist between three samples derived from the same drill hole.

Carbonate reactions with evolved HCl were likely not significant contributors to evolved CO_2 detections (Figure S7 in Supporting Information S1). Evolved HCl reactions with carbonate can lower the thermal decomposition temperature of carbonates (Cannon et al., 2012). However, the most intense CO_2 peaks in most samples evolved at temperatures lower than the most intense HCl peaks suggesting that such reactions were not significant contributors to evolved CO_2 . The NT2 and EB samples had low intensity evolved HCl peaks at 300°C and 330°C, respectively, that may have contributed to some evolved CO_2 from carbonate. HCl was mostly evolved at higher temperatures where carbonates typically undergo thermal decomposition suggesting that HCl/carbonate reactions did not have a major role in evolving the detected CO_2 .

High temperature (~800°C) CO_2 with coevolving CO observed in the GG2 and NT2 sample data strengthened the argument that oxidized organics sourced CO_2 at those temperatures (Figures 9a and 9b). While not necessary, the presence of co-evolving CO can strengthen the case for organic C because CO is not released from the thermal decomposition of carbonate (e.g., Sharp et al., 1991).

4.3.3. High Temperature CO_2 , CO, and SO_2

The co-evolution of CO_2 , CO, and SO_2 at high temperature may indicate the presence of a sulfate-oxidized C phase in all samples (Figure 9), though the nature of this association is unclear based on EGA data. Sulfates precipitated in the presence of organic C may subsequently aid in organic C preservation by physically limiting

exposure to oxidative processes in the subsurface. Such association could manifest as concurrent CO₂, CO, and SO₂ evolution upon thermal decomposition of the sulfate (Aubrey et al., 2006; Eigenbrode et al., 2018; Francois et al., 2016; Lewis et al., 2015). Evolved CO₂ and CO observed between 500°C and 600°C in all GG and NT samples fell within the temperature range of the main Fe-sulfate SO₂ peak suggesting that while CO₂ and CO did not perfectly align with the main SO₂ peak at these temperatures, Fe-sulfates could have contributed to preserving organic C. Co-evolved CO₂, CO, and SO₂ peaks (~690°C) in EB were consistent with organic C preservation in either Fe-sulfate or Mg-sulfate. Co-evolving CO₂, CO, and SO₂ at 800°C in GG2 and NT2 were consistent with Mg-sulfate preservation of organic C while the HU co-evolution temperatures were consistent with Fe-sulfate preservation of organic C with no evidence of preservation by Mg-sulfate. Organic C preservation in Ca-sulfate detected by CheMin was possible but the SAM oven was not designed to achieve temperatures needed to decompose Ca-sulfate (>1100°C).

Several possible scenarios could explain the C-S associations detected by the SAM. Sulfates in GT are largely diagenetic precipitates (e.g., O'Connell-Cooper et al., 2022; Thompson et al., 2022; Thorpe et al., 2022); thus, dissolved organics during sulfate precipitation would be necessary to establish organic encapsulation or surface adsorption that may be responsible for the high temperature C-S release. Such conditions would have been possible if groundwater bearing the sulfate ions also carried diagenetic products of weathered macromolecular carbon or microbial products from a groundwater ecology. The C-S association observed could also be related to a trace phase in the samples that have little to do with the depositional conditions, and more to do with formation within meteorites or lithic grains maintaining a record of mafic processes (e.g., Steele et al., 2012, 2016). A third possibility is that the observed concurrent CO₂, CO, and SO₂ high temperature releases are related to poorly understood C-S thermochemical conditions in the SAM oven and not directly representative of sample features.

4.3.4. MTBSTFA/DMF Background

Evolved CO could have contributions from the carbonyl containing derivatization agents MTBSTFA/DMF brought for SAM-GCMS wet chemistry analyses. Masses attributed to products of MTBSTFA/DMF thermal decomposition (e.g., formaldehyde m/z 29; HCN m/z 27) (Glavin et al., 2013; Stern et al., 2015) all have significant evolutions that coincided with the most intense evolved CO peak in all samples (Figure S8 in Supporting Information S1). The sum of evolved formaldehyde and HCN created a peak that was similar in shape to the evolved CO (Figure S8 in Supporting Information S1). However, evolved CO at higher temperatures above the main CO release were not associated with any MTBSTFA decomposition byproducts (Figure S8 in Supporting Information S1).

The lack of HCN and formaldehyde byproducts at high temperatures suggests that evolved CO releases at high temperatures (>450°C) do not have contributions from MTBSTFA and DMF byproducts. This high temperature CO was instead attributed to evolved C indigenous to the sample.

Unlike CO, CO₂ did not correspond exactly to evolution of MTBSTFA and DMF decomposition byproducts; however, the possibility exists that MTBSTFA and DMF decomposition could evolve CO₂ (Freissinet et al., 2015; Glavin et al., 2013; Stern et al., 2022). Total C contributions from MTBSTFA and DMF were estimated to be ~2 μmol C per run (Freissinet et al., 2015). However, this estimate was based on experiments in the presence of evolving O₂ from oxychlorine that act to combust MTBSTFA. Oxychlorine was not detected in the Gm samples suggesting that background contributions to evolved CO₂ could be much lower than 2 μmol C per run. However, the EB sample did evolve oxychlorine O₂ and could have as much as 2 μmol contribution to the 15.5 μmol of CO₂ detected in EB (Table S6 in Supporting Information S2).

Despite the presence of background carbon, Martian carbon can still be present at low temperatures. Isotopic evidence from the combustion experiments demonstrated that indigenous Martian C was evolved from the Cumberland sample at low temperatures (Stern et al., 2022). MTBSTFA/DMF could have contributed to evolved CO₂ below 550°C but Martian sources of evolved CO₂ were still present. The isotopic composition ($\delta^{13}\text{C} = 1.5\text{‰} \pm 3.8\text{‰}$) of carbon evolved (950 μg C/g) at low temperatures strongly suggested the presence of a ¹³C enriched indigenous C source mixed with depleted instrument background carbon ($\delta^{13}\text{C} -35\text{‰}$) (Stern et al., 2022).

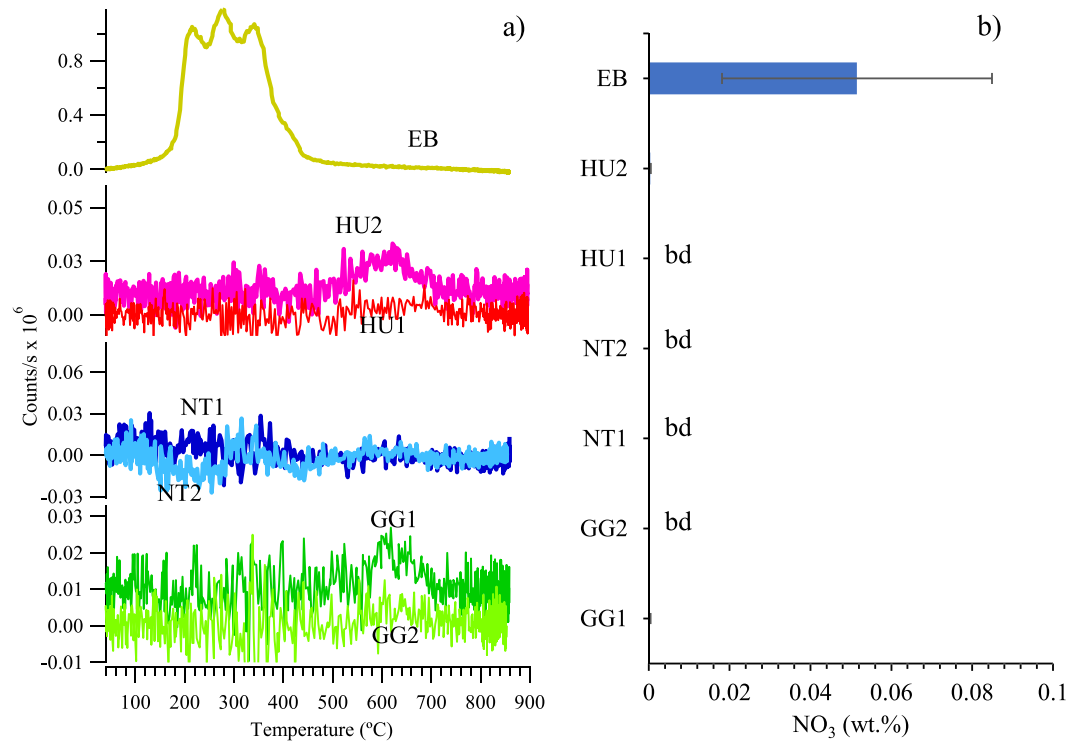


Figure 10. (a) Evolved NO (m/z 30) versus temperature. (b) Total nitrate abundance derived from total evolved NO. Below detection limits (bd).

4.4. NO

Nitrate was detected in EB sandstone but was mostly absent in the Gm mudstones. The Gm mudstones were characterized by undetectable (<0.001 wt.% NO_3) to very low levels of NO in two samples (GG1, HU2) (Figure 10, Table S8 in Supporting Information S2). Undetectable levels of evolved NO were common throughout the GT trough and VRR (except Rockhall) (McAdam et al., 2020, 2022). Contrary to the Gm samples, the EB sandstone, when compared to previous samples, had the second highest nitrate detection (0.06 wt.% in EB vs. 0.07 wt.% in Cumberland) (Sutter et al., 2017). The evolved NO from EB was characterized by a multipeak release that occurred between 150°C and 450°C which was consistent with multiple nitrate phases being present. Evolved NO releases were consistent with contributions from Fe-nitrate (Stern et al., 2015) though other nitrate phases cannot be excluded because nitrate-metal oxide mixtures (e.g., Fe-oxides) can reduce nitrate thermal decomposition temperatures (Hoshino et al., 1981). The origins of Martian nitrate are believed to be derived from atmospheric N_2 fixation caused by volcanic lightning, ultraviolet light, and bolide impacts on early Mars (Manning et al., 2009; Segura & Navarro-González, 2005; Summers & Khare, 2007).

4.5. O₂

Evolved O₂ was undetectable in the GG, NT, and HU samples but was detected in the EB sample (Figure 11, Table S9 in Supporting Information S2). The undetectable levels of O₂ were consistent with oxychlorine (chlorate or perchlorate) occurring below SAM detection limits (<0.001 wt.% ClO_4) in the GG, NT, and HU samples. Oxychlorine abundance is reported as perchlorate (ClO_4) for simplicity and ease of comparison to previous results (e.g., Sutter et al., 2017; McAdam et al., 2020, 2022) though presence of chlorate (ClO_3) is a strong possibility (see below). Evolved O₂ was detected in the EB sample (0.13 wt.% ClO_4) and was represented by a lower intensity peak ($\sim 160^\circ\text{C}$) followed by a higher intensity peak ($\sim 315^\circ\text{C}$). Unlike nitrate, the amount of oxychlorine detected was similar to most oxychlorine abundances from previous sedimentary rock samples (Sutter et al., 2017).

Evolved O₂ release temperatures in EB were consistent with the presence of sodium or magnesium chlorate (NaClO_3 , MgClO_3). Comparison of evolved O₂ release temperatures in EB with laboratory studies suggest that

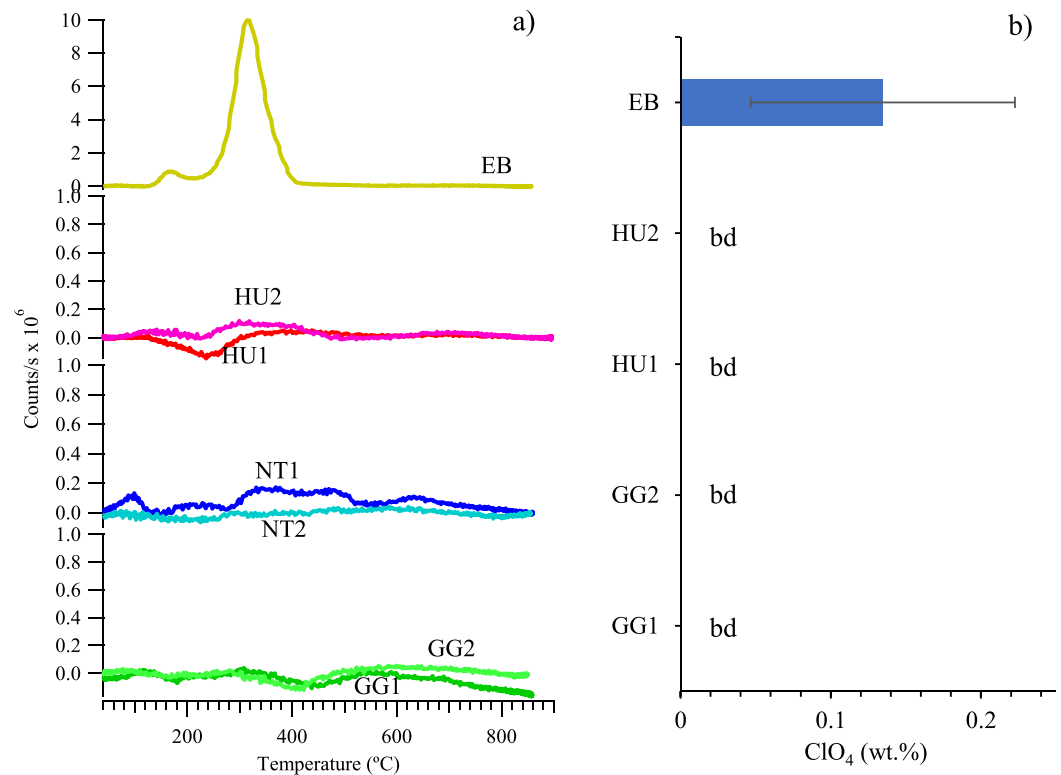


Figure 11. (a) Evolved O₂ (m/z 32) versus temperature. (b) Total perchlorate (ClO₄) abundances as derived from total O₂ abundances. Below detection limits (bd).

sodium or magnesium chlorate mixed with ferrihydrite both evolved O₂ consistent with the EB O₂ release temperatures (Hogancamp et al., 2018) (Figure S9 in Supporting Information S1). Laboratory thermal decomposition studies have demonstrated that Fe-oxide phases serve to lower the thermal decomposition temperature of pure chlorates and perchlorates (Furuichi et al., 1974; Hogancamp et al., 2018; Rudloff & Freeman, 1970). Poorly crystalline phases similar to ferrihydrite were likely present as demonstrated by the presence relatively broad ~240°C H₂O peak consistent with amorphous Fe in EB (Figure 5). The EB evolved O₂ detections could be the result of the reactions between these poorly crystalline Fe phases and chlorate (Hogancamp et al., 2018). Mg-perchlorate mixed with ferrihydrite evolved O₂ at higher temperatures than chlorate suggesting that evolved O₂ from Mg-perchlorate was a less favorable candidate than Mg-chlorate or Na-chlorate (Figure S9 in Supporting Information S1). Laboratory evaluation of Na-perchlorate mixtures with iron oxides has not been conducted so the presence of Na-perchlorate cannot be excluded, especially considering the confirmed Raman spectroscopic detection of Na-perchlorate in Jezero Crater (Farley et al., 2022).

4.6. HCl

Evolved HCl for the GG, NT HU, and EB samples had a broad two peak release from 300°C to 870°C (Figure 12) that was attributed to NaCl. The two most intense HCl releases in GG and EB were similar with peaks at ~520°C and ~730°C. The double peak evolution profile was similar to the HU and NT samples, though the HU and NT samples had lower and higher first peak temperatures, respectively. The HU HCl first peak occurred at lower temperature (460°C) while the second peak temperature was similar to the GG and EB samples. The NT HCl release pattern was mostly characterized by single broad peak (600°C) with subtle higher temperature peak (800°C).

The double peak nature of evolved HCl releases were consistent with thermal decomposition of NaCl in the presence of evolved water from thermally dehydroxylating phyllosilicate in these samples. Laboratory SAM-EGA analog analyses of NaCl and nontronite mixtures yield similar evolved HCl release patterns to those detected in the Gale crater samples (Figure S10 in Supporting Information S1) (J. V. Clark et al., 2020). The HCl production

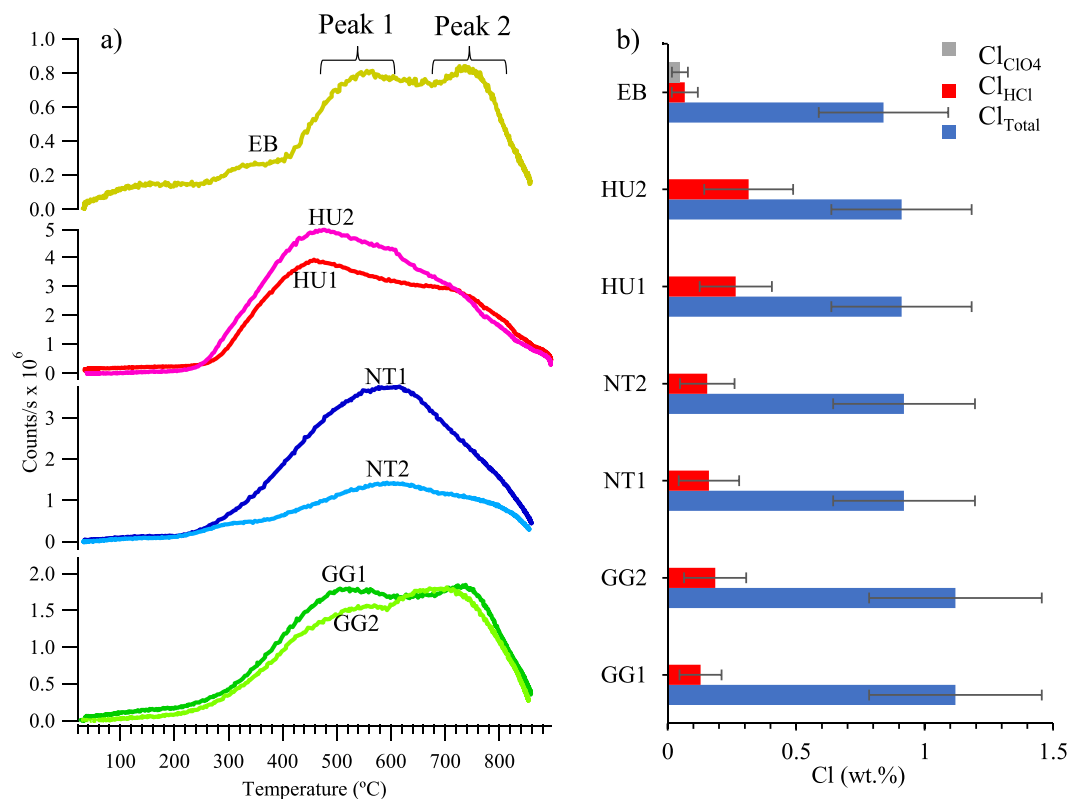


Figure 12. (a) Evolved HCl (m/z 36) versus temperature as detected by Sample Analysis at Mars-evolved gas analyzer (SAM-EGA). (b) Total chlorine content from evolved HCl detected by the SAM-EGA (Cl_{HCl}), total chlorine calculated from evolved O_2 as perchlorate (Cl_{ClO_4}), and total Cl as detected by Alpha Particle X-ray Spectrometer (Cl_{Total}).

is the result of water vapor reaction with melted NaCl. Mixing effects of NaCl with salts and nontronite act to lower the melting temperature of NaCl to permit reaction (1) to occur at temperatures below the standard NaCl melting temperature. Not all NaCl will react at lower temperatures and unreacted NaCl will melt near its typical melting temperature ($\sim 800^\circ C$) resulting in the observed double HCl peak (Figure 12, Figure S10 in Supporting Information S1).



The EB sample had an additional lower temperature HCl release ($330^\circ C$) that could be derived from Mg-chlorate (discussed above). Mg-chlorate thermal decomposition results in the co-evolution of O_2 and HCl suggesting that co-evolving O_2 and HCl from EB could be consistent with Mg-chlorate (Hogancamp et al., 2018).

Evolved HCl abundances were mostly similar in the GG, NT, and HU samples while the EB trended lower than the other samples (Figure 12b, Table S10 in Supporting Information S2). Total APXS Cl abundances were similar between the GG, NT, HU, and EB samples and were always greater than HCl abundances. This was expected because the reaction efficiency between NaCl (< 1 wt.%) and water vapor was expected to be less than 100% because of competing water absorption onto other phases; thus restricting water vapor contact with NaCl during SAM-EGA analysis.

5. Discussion

5.1. H_2O

The lower Fe-smectite abundance in HU compared to GG and NT was attributed to post-depositional alteration processes in HU that lowered the initially higher smectite abundances in HU. This observation was consistent with acidic alteration of Fe-smectite to amorphous Fe and cristobalite in HU. Evidence of higher abundances of

amorphous Fe-phases in HU was indicated by the intense $\sim 220^\circ\text{C}$ peak (consistent with poorly-crystalline FH decomposition) that dominated the low temperature evolved water in HU. Laboratory batch and flow-through acidic (pH 0–4) alteration studies of nontronite demonstrated the degradation of nontronite resulted in the formation of amorphous silica and solution chemistry consistent with precipitation of Fe-oxyhydroxides (e.g., Altheide et al., 2010; Gainey et al., 2014; Gates et al., 2002). The lack of kaolinite formation and silica loss typically associated with terrestrial open-alteration scenarios (e.g., Baker & Neill, 2017; Fisher & Ryan, 2006; Ryan & Huertas, 2009; Sherman et al., 1962; Vingiani et al., 2004) suggested that acidic conditions inhibited kaolinite formation and restricted flow inhibited silica loss. This caused silica to become oversaturated and allowed for cristobalite and opal-CT formation. The detection of apatite and magnetite in HU suggested that acidic activity was short lived unless apatite and magnetite were secondary and formed after the acidic alteration events. Short-lived acidic activity was proposed for apatite detections in jarosite containing sediments in the Pahrump Hills encountered by the rover earlier in the mission (Rampe et al., 2017).

Alternatively, Si-poor sulfate brines not requiring low pH could have destabilized Fe-smectite in HU and promoted the formation of amorphous Si and Fe phases (Bristow et al., 2021). The low smectite clay contents in the VRR samples Duluth, Storer, Highfield, and Rockhall were proposed to be a result of late-stage diagenesis involving Si-poor sulfate brines derived from overlying sulfate strata that infiltrated into VRR sediments prior to lithification (Bristow et al., 2021). The low Si-activity of the brines promoted Fe-smectite dissolution resulting in the formation of amorphous Si and Fe phases. Further diagenetic processes transformed the amorphous Si to cristobalite and opal-CT.

The detrital deposition of smectite, while possible, was not favored for the EB sandstone. Terrestrial detrital clay (smectite) sources include percolating clay rich waters or eolian deposition of clay rich dust onto a wetted surface sand to form clay coatings (Worden & Morad, 2003). These clay sources were difficult to reconcile for the Gp capping unit because, clay rich waters percolating into sandstones are usually associated with fluvial settings which was unlikely for the dry eolian environment that deposited the Gp capping unit (Banham et al., 2022; Bedford et al., 2022). Eolian deposition of clay rich coatings on sand grains also was not favored because Martian dust does not contain smectite (e.g., Bish et al., 2013; Blake et al., 2013).

The EB smectite was likely derived by post-depositional alteration of the Gp capping unit. Aqueous alteration of terrestrial eolian sand to form clays is known (e.g., Worden & Morad, 2003). Smectite detected in the Windjana and Oudam sandstones, lower down Mt. Sharp, were proposed as being derived from post-depositional aqueous alteration scenarios (Achilles et al., 2020; Treiman et al., 2016). Reactive phases (olivine and pyroxene) in EB likely served as parent minerals for smectite formation. The detection of low smectite concentration and the persistence of olivine in EB was consistent with short-lived aqueous alteration. Alteration of basaltic material under limited flow and permeability commonly leads to smectite forming first in terrestrial settings (Baker & Neill, 2017; Benson & Teague, 1982; Fisher & Ryan, 2006; Ryan & Huertas, 2009; Vingiani et al., 2004). Smectite formation may have contributed to cementation of the EB sandstone and the overall resistant nature of the Gp capping unit similar to processes proposed for the cementation of the smectite containing Windjana sandstone (Bedford et al., 2022; Treiman et al., 2016). Furthermore, smectite was not detected in the Sf at the Emerson and Naukluft plateaus, which may relate to differences in fluid pH, supporting that the fluids that cemented the Gp capping unit were derived from a different source (Bedford et al., 2022).

5.2. SO_2

Fe and Mg-S phases amounted to 5%–19% of the total S indicating that CaSO_4 dominated the S phases in the Gm and EB materials. The dominance of Ca-sulfate suggested sulfur geochemistry was mostly controlled by Ca-sulfate bearing fluids with some contributions from Fe and Mg-sulfate. The low abundances of Fe and Mg-sulfate compared to CaSO_4 in these materials was like most samples in other parts of Gale crater (e.g., McAdam et al., 2020, 2022; Sutter et al., 2017) demonstrating the ubiquitous nature of Ca-sulfate in many Gale crater units.

The lower SAM-S and APXS-S abundances in HU (Figure 6b, Table S5 in Supporting Information S2) were consistent with leaching loss of sulfate by S poor fluids in HU. Higher SAM-S and APXS-S abundances in the GG and NT sediments indicated these materials were not exposed to the same alterations processes that removed

S from HU. The lack of soluble Mg-sulfate in HU that was detected in the GG and NT samples would also be consistent with leaching loss of highly soluble Mg-sulfate from HU.

The relatively unfractionated $\delta^{34}\text{S}$ values for GG and NT contrasted against the highly enriched HU $\delta^{34}\text{S}$ values and were consistent with HU exposure to sulfur bearing fluids enriched in ^{34}S after deposition (Table S5 in Supporting Information S2). Several reaction mechanisms were possible that enriched the sulfur sources with ^{34}S (e.g., Franz et al., 2017) and determining which mechanism was responsible for creating enriched ^{34}S sources was beyond the scope of this work. The initially deposited HU sulfur could have had an unfractionated $\delta^{34}\text{S}$ signature similar to GG and NT. Subsequent alteration of HU by enriched ^{34}S solutions diluted the initially deposited unfractionated $\delta^{34}\text{S}$ values with enriched $\delta^{34}\text{S}$ values. Alternatively, earlier leaching losses of S with unfractionated $\delta^{34}\text{S}$ values could have been replaced by later deposition of S with enriched $\delta^{34}\text{S}$ values. A similar ^{34}S enriching process lower down Aeolis Mons occurred in the Murray formation (Mf) mudstone Buckskin (BK) sample (20 cm below SPg unconformity) (Yen et al., 2021). The BK $\delta^{34}\text{S}$ was enriched (25‰–28‰) relative to the lower Telegraph Peak (6 m below SPg unconformity) sample that was less enriched ($\delta^{34}\text{S} = 6\text{‰}–8\text{‰}$) (Franz et al., 2017; Yen et al., 2021). Similar to HU, post-depositional alteration processes resulted in the ^{34}S enrichment of the BK sample.

Sulfur fluid exchange between HU and EB was not evident which contrasted with evidence of S fluid exchange at the SPg unconformity between Mf and Sf sediments lower down Aeolis Mons (Yen et al., 2017) (Figure S12 in Supporting Information S1). The high temperature evolved SO_2 peak ($\sim 875^\circ\text{C}$) observed in Greenhorn (GH), BS, and BK suggested that similar MgSO_4 bearing fluids had moved between the 6–7 m of Sf sandstone (BS and GH) above and at least 0.2 m of Mf (BK) material below the unconformity (Figure S12 in Supporting Information S1). EB and HU are 5 m above and 1.7 m below the unconformity, respectively. The evolved SO_2 release pattern for the EB and HU samples did not demonstrate any similarities like those observed for BS, GH, and BK suggesting sulfur fluid movement did not move to the same extent between Sf and Gm mudstones in the GT trough region (Figure 6).

The contrasting $\delta^{34}\text{S}$ values between the HU and the EB samples (Table S5 in Supporting Information S2) was also consistent with limited S exchange between the two localities. The heavily depleted $\delta^{34}\text{S}$ value from EB (-27‰) was distinctly different from the enriched HU and unfractionated $\delta^{34}\text{S}$ values for GG and NT (Table S5 in Supporting Information S2). These contrasting $\delta^{34}\text{S}$ values were consistent with the EB sulfur being derived from a different S source than the Gm samples and that S exchange did not extend the full 6–7 m between EB and HU. This was counter to the similarly enriched $\delta^{34}\text{S}$ values for both the BK (Mf mudstone) and BS/GH (Sf) samples that supported extensive S fluid movement of 6–7 m between Sf sandstone and Mf mudstone lower down Aeolis Mons (Yen et al., 2017).

Evidence of reduced sulfur (likely iron sulfide) in EB suggested that EB may exist in state of redox disequilibrium. Direct detection of reduced sulfur (i.e., co-evolving O_2 and SO_2) suggestive of oxidation of reduced sulfur was detected in EB but not the Gm samples. Quadratic discriminant analysis also suggested evidenced of reactions between Fe-sulfide with evolved CO_2 in EB (Wong et al., 2022). The low intensity of the evolved SO_2 at 300°C indicated that reduced sulfur consists of a minor fraction of the total EB sulfur. Nevertheless, reduced sulfur in the presence of detected sulfate, demonstrated that EB exists in a state of redox disequilibrium. Redox disequilibrium in EB may be the result of limited and short-lived aqueous alteration that inhibited EB from achieving complete sulfur oxidation.

5.3. Carbon (CO_2 and CO)

5.3.1. Gm CO_2/CO

5.3.1.1. Gm Low Temperature ($<450^\circ\text{C}$) CO_2/CO

The C abundances were similar within error in the Gm materials suggesting that alteration processes that affected the HU materials did not significantly affect organic C concentration attributed to macromolecular carbon and Fe-oxalates. Evaluation of the most intense CO_2 and CO peak release temperatures and abundances did not show any major differences between GG, NT, and HU samples. The most intense CO_2 peak release pattern in NT1 differed from NT2 but the similarity of NT2 with the GG and HU samples suggested that the NT2 was more representative of the overall C in NT. The similarity of the evolved CO_2 and CO in GG, NT, and HU suggested

that alteration processes being proposed for the HU sample did not have a significant effect on decreasing or increasing the types or abundance of C in the HU sample.

Organic C preservation by abundant amorphous materials in the Gm samples (37–47 wt.%; X-ray amorphous materials; Table S3 in Supporting Information S2) may have acted to stabilize organic C in materials (e.g., Egli et al., 2008; Filimonova et al., 2016) preventing losses through alteration processes. Carboxylated organic carbon is known to bond to Al- and Fe(III)-hydroxyl groups through ligand exchange (e.g., Boily et al., 2007; Sposito, 1989). Instead of organic salts (e.g., acetates, oxalates) that are less stable under acidic alteration conditions proposed for HU, stabilized organic C complexes may have formed with amorphous Al- and Fe-hydroxides preventing loss of C from HU. Furthermore, acidic solutions proposed in the alteration of HU could have favored hydrated metal sites (Lewis acid sites) that were more favorable for organic carbon ligand exchange reactions on Al- and Fe-hydroxide surfaces (Sposito, 1989).

Macromolecular C that dominates (70%–80%) carbonaceous chondrite meteorites (e.g., Robert & Epstein, 1982) could be another contributing source of C to the Gm sediments. Macromolecular C is defined as “insoluble” to acid dissolution (Robert & Epstein, 1982) and if initially deposited in Gale crater, would resist leaching and could explain the minimal differences in organic C concentrations between the more altered HU and less altered GG and NT materials. As indicated earlier, combustion analysis of the Cumberland sample demonstrated that reduced hydrocarbons persisted in Cumberland and the presence of diverse hydrocarbon structures released at high temperatures from Mf mudstones suggested that ionizing radiation has not completely oxidized all organic C phases in Gale materials (Eigenbrode et al., 2018; Stern et al., 2022). Initially deposited macromolecular organic C could, through billions of years of ionizing radiation, have been partially oxidized (e.g., Benner et al., 2000) and, therefore, could have contributed to evolved CO₂ and CO detected in the Gm sediments.

5.3.1.2. Gm High Temperature (>450°C) CO₂/CO

Alteration processes expected for HU did not appear to have affected high temperature C abundances. High temperature (>450°C) evolved C consisted of possible contributions from Na-, K-, Ca-, Mg-oxalates, carbonates, trapped CO₂ gas in glass, an ill-defined C-sulfate phase, and larger more refractory macromolecular C. Alteration processes proposed for HU include acidic solutions that are expected to result in the loss of carbon from oxalate and carbonate, as well as potentially the alteration of glass containing CO₂. However, the variable peak intensity between the Gm materials that could be attributed oxalate, carbonates, a C-sulfate phase, and trapped CO₂ make it difficult to see any trends that may suggest HU alteration processes affected the presence of such phases. Detecting any trends was further complicated by such low abundance of C at these temperatures as indicated by lower peak intensities relative to higher intensities below 450°C.

5.3.2. Sf, Edinburgh CO₂/CO

The three evolved CO₂ peaks from EB suggested that the type and distribution of low temperature C phases in EB differed from the Gm materials. All peaks could be attributed to macromolecular C that may have different composition that resulted in the EB sample's triple peak nature rather than the broad CO₂ peak in the Gm materials. Despite lower amorphous content in EB, poorly crystalline Fe(III)- and Al-hydroxides could have role in preserving organic C in EB. Possible sources of differing carbon composition could be related to differing sediment sources associated with EB versus the Gm materials. All Gm materials have undergone more alteration than EB which could affect the organic C chemistry and thus the evolved CO₂ temperatures. The higher carbon concentration detected in EB was also consistent with limited alteration in EB that would serve to preserve carbon in EB over the more altered Gm materials.

Similar to the detection of reduced S, possible siderite detection adds more support to redox disequilibrium in EB. The 425°C CO₂ peak could have contributions from Fe(II)-carbonate (e.g., siderite) (Figure S5 in Supporting Information S1). The high magnetite and low hematite abundances (Table S3 in Supporting Information S2) coupled with the low temperature (~330°C) evolved SO₂ consistent with Fe-sulfide (Figure 6) suggested that fluid conditions were suboxic, which may have favored siderite stability in EB. If the evolved 425°C peak was attributed to siderite it would have been below CheMin detection limits. The possible presence of siderite and iron sulfide coupled with the detection of sulfate, oxychlorine, nitrate, and chloride were consistent with a state of redox disequilibrium resulting from short-term limited aqueous alteration in EB.

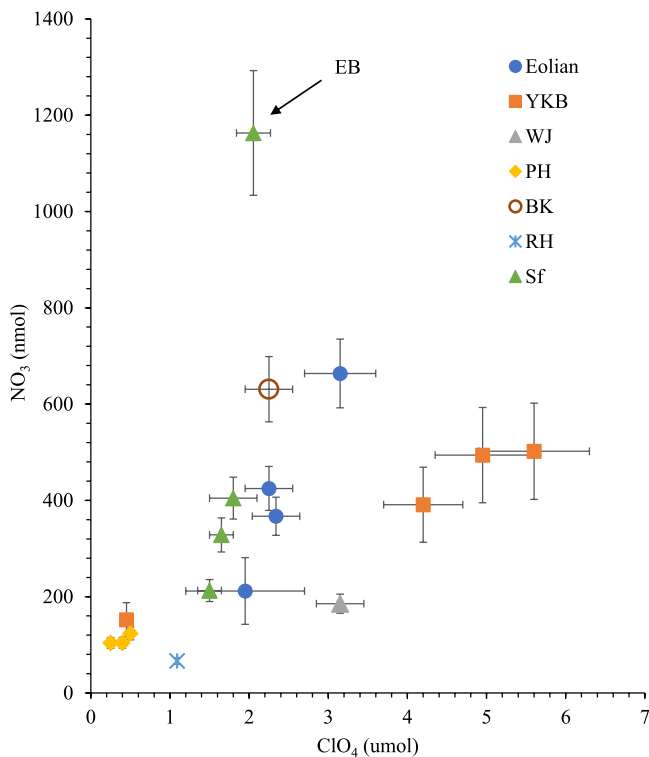


Figure 13. Total nitrate versus total perchlorate abundances in Gale crater as derived from total NO and O₂ by Sample Analysis at Mars-evolved gas analyzer. Legend abbreviations indicated are Yellowknife Bay (YKb) (includes Cumberland, John Klein), Windjana (WJ), Pahrump (PH) (includes Confidence Hills, Mojave, and Telegraph Peak samples), Buckskin (BK), Rockhall (RH), and Stimson sandstone samples (Sf) (includes Big Sky, Greenhorn, and Edinburgh [EB]). The EB sample is indicated with arrow. See Table S11 in Supporting Information S2 for data.

Low intensity CO₂/CO peaks at temperatures above 500°C were consistent with the relatively minor presence Ca/Mg carbonate, Ca/Mg oxalate, CO₂ trapped in glass, and larger more refractory carboxyl/carbonyl containing macromolecular C. Co-evolving SO₂ with CO₂ at ~700°C suggests the possibility of preserved organic C in an Fe/Mg sulfate (Figure 9d).

5.4. Nitrate/Oxychlorine/Chloride

The non-detection of oxychlorine and limited nitrate in the GG, NT, and HU samples was consistent with limited deposition of these phases or that post-depositional processes leached these soluble salts from the sediments. Post-depositional diagenetic processes that operated in the GG, NT and HU sediments could have leached initially deposited soluble nitrates and oxychlorine before erosion of the Gm sediments. However, in all cases, Cl (likely chloride) was detected by SAM and APXS instruments (Figure 12, Table S10 in Supporting Information S2) suggesting leaching solutions if responsible for nitrate and oxychlorine loss, contained soluble chloride but lacked nitrate and oxychlorine. All soluble salts could also have been leached and later solutions containing only chloride salts returned chloride to the sediments. Nitrate and oxychlorine may have, alternatively, never been deposited in GG, NT, and HU. Similar to the Gm, samples limited to undetectable nitrate and oxychlorine has also affected over ~325 m of stratigraphically lower samples that span the GT trough, the VRR, down to the Oudam sample below the VRR (J. Clark et al., 2021; J. V. Clark et al., 2020; McAdam et al., 2020). This suggests that processes that have affected nitrate and oxychlorine abundance in Gm has been widespread as it has affected other sediments as well.

Nitrate and oxychlorine have consistently been detected in Sf material. The EB sample in the Gp capping unit unlike the GG, NT, and HU samples, had the second highest level of nitrate (0.06 wt.% NO₃) encountered by the rover in Gale crater (as of sol 3333) and had detectable O₂ that was consistent with oxychlorine species. Nitrate and oxychlorine were also detected in the BS and altered GH Sf samples (Sutter et al., 2017) indicating that oxychlorine and nitrate deposition was common to the Sf samples. Stimson cementation fluids contained nitrate and oxychlorine and post-depositional alteration was likely limited in nature which resulted in limited nitrate and oxychlorine leaching losses.

tation fluids contained nitrate and oxychlorine and post-depositional alteration was likely limited in nature which resulted in limited nitrate and oxychlorine leaching losses.

The extent of nitrate and oxychlorine fluid exchange between EB and the Gm sediments was likely limited. The non-detection of oxychlorine and limited detection of nitrate in Gm sediments coupled with oxychlorine and nitrate detections in EB suggested that these soluble salts did not infiltrate down to the HU sample 1.7 m below the Gp capping unit. This was counter to what was observed at the SPg unconformity between the Sf (BS and GH) and Mf (BK) samples. In addition to sulfate (discussed above), nitrate, and oxychlorine exchange between the Sf and Mf material was apparent (Yen et al., 2021; Figure S12 in Supporting Information S1) suggesting that fluid exchange transited the 6–7 m between the Sf and Mf materials during or after the deposition of the Sf sandstone. Observed cross-cutting fractures acted as fluid conduits between Sf sediments and the BK sample but were not observed between the Gp capping unit and the Gm mudstone in the HU region. The lack of cross cutting fractures in the HU region could have contributed to preventing salt exchange between the HU and Gp capping unit materials.

Processes that affected the distribution of nitrate and oxychlorine in EB appeared to have differed for EB compared to other Sf samples. The EB sample had a much higher nitrate/oxychlorine ratio compared to previous Sf samples lower down Aeolis Mons as well as other Gale crater samples (Figure 13, Table S11 in Supporting Information S2). Without EB, nitrate and oxychlorine were weakly correlated (improving the R² from 0.23 to 0.51) in the remaining the Gale crater samples. The correlation and significantly lower ratios suggested that processes responsible for nitrate/oxychlorine production and loss achieved a steady state over the time of sediment deposition in most Gale samples except in EB. Another possibility was that initially variable nitrate and

oxychlorine deposition and loss rates were averaged. Post depositional fluvial, eolian, aqueous or other processes could have redistributed and averaged the nitrate/oxychlorine ratios to the observed lower values except in EB (Stern et al., 2017). This would be consistent with limited post-depositional processes in EB that could have lowered the EB nitrate/oxychlorine ratio.

The higher nitrate/oxychlorine ratio in EB (relative to BS/GH) could also be the result of chemical differences between surface waters that may have cemented EB and the groundwaters that cemented the lower BS and GH Sf sediments. The fan-shaped morphology of the Gp at the base of the Gediz Vallis ridge has been attributed to surface waters eroding the slope of Aeolis Mons (Bedford et al., 2022). The lower Sf samples BS and GH were likely cemented by groundwater (Banham et al., 2018). Groundwater interactions dominating in the BS and GH could be attributed to lower elevation and/or older age when groundwater processes may have been more active than when EB was deposited (Bedford et al., 2022). Alteration fluid chemical differences between BS and EB were indicated by lower S in EB than in BS and presence and absence of smectite in EB and BS, respectively. The differing alteration mineralogies coupled with the differing nitrate/oxychlorine ratios would be consistent with fluid chemical differences between surface waters that cemented EB and groundwaters that cemented BS and GH.

5.5. Siccar Point Unconformity Alteration Scenarios

Subsurface diagenetic alteration of the HU material after SPg emplacement over Gm is a plausible scenario to explain observed SAM-EGA results (Figure 14). Following the scenario described in Figure 14.

1. Sediment members of the CSf were deposited in stratigraphic order of Gm, Mm, and then Pm.
2. Drying of the Gm mudstone resulted in observed fractures (e.g., Figure 3a). The Gm, Mm, and Pm materials were eroded. Erosion of the Gm surface resulted in the HU layers being close to the eroded surface while the GG and NT layers remained further from the eroded surface and beyond the reach of alteration processes that affected HU. The low nitrate and non-detection of oxychlorine phases in GG, NT, and HU as well as all other GT trough samples (McAdam et al., 2022) suggests that if these phases were ever deposited, diagenetic processes leached these soluble phases from all GT sediments before the formation of the SPg unconformity. Alternatively, these phases were never deposited in sufficient quantity to be widely detected by SAM except in few cases regarding limited nitrate detections.
3. Eolian sand was deposited over the eroded Gm, Mm, and Pm surfaces. The sand was cemented forming the SPg, but cementation fluids did not penetrate significantly into the HU materials. The resulting SPg material consisted of a relatively high C content. Sulfur was derived from sources heavily depleted in ^{34}S . The SPg material was cemented from surface waters that permitted limited smectite formation in EB. However, alteration was not enough to significantly leach initially deposited C, nitrate, and oxychlorine. Evidence of possible siderite, reduced sulfide, along with magnetite and oxidized sulfate, nitrate, and oxychlorine phases suggested that EB alteration may have been short-lived to permit the persistence of redox disequilibrium in EB. The presence of nitrate/oxychlorine in EB but not HU was consistent with SPg unit alteration/cementation fluids that did not penetrate the Gm materials. Depleted and enriched $d^{34}\text{S}$ values in EB and HU, respectively, were also consistent with limited exchange of S fluids between SPg and Gm sediments. However, the presence of highly depleted CH_4 - $d^{13}\text{C}$ values detected in SAM analyses of HU and EB suggested that fluid exchange of this carbon may have occurred between HU and EB (House et al., 2022).
4. Upwelling acidic groundwaters moving through Gm fractures to the SPg contact and subsequently migrated along the contact altering the HU smectite to amorphous Si and Fe-rich material. The acid-buffering nature of basaltic material was largely bypassed as fluids moved through fractures that limited fluid contact with the basaltic sediments. Amorphous Si eventually crystallizes to cristobalite and opal-CT (Table S3 in Supporting Information S2). Sulfuric acid fluids were derived from a groundwater source enriched in ^{34}S that acted to replace previously unfractionated sulfur with sulfur enriched in ^{34}S . Upwelling acidic diagenetic fluids that concentrated along the SPg contact have also been invoked for observed alteration chemistry and mineralogy at the BK (~20 cm below SPg contact) as well as VRR samples proposed to have resided below the SPg unconformity (Rampe et al., 2020; Yen et al., 2021). The upwelling acidic fluids flowed through fractures that minimized contact with acidic neutralizing nature of the basaltic sediments. If acidic groundwaters are invoked, then magnetite detected in HU would likely have formed during some event after acidic alteration. Furthermore, Fe and Mn veins that have been proposed to have formed before erosion of the Gm (Gasda

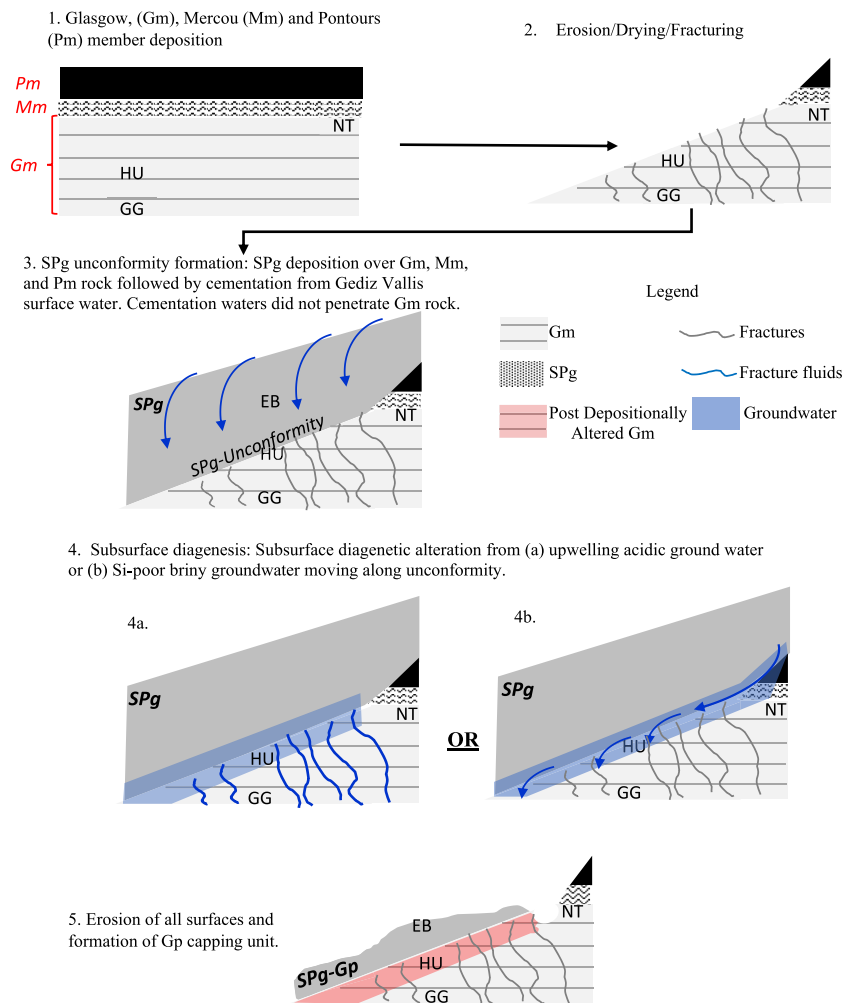


Figure 14. Proposed alteration scenario(s) for Sample Analysis at Mars-evolved gas analyzer detected chemistry and mineralogy detected in Hutton (HU) and Siccar Point group (SPg) materials. Glasgow (GG), Nontron (NT), Edinburgh (EB), and Greenheugh pediment (Gp) capping unit.

et al., 2022) would under this acidic alteration scenario, be unstable and thus likely have formed after SPg deposition and subsequent acid alteration proposed here.

5. Instead of acidic alteration fluids, Si-poor sulfate brines migrating along the SPg contact derived groundwater sources from stratigraphically higher sulfate deposits could plausibly have destabilized Fe-smectite resulting in amorphous Fe and opal-CT and cristobalite formation. This process was invoked for lower Fe-smectite concentrations of VRR samples relative to the GT trough samples (e.g., Kilmalie, Aberlady, and Glen Etive) (Bristow et al., 2021). The influx of sulfate brines in this scenario could have sourced the sulfate enriched in ^{34}S that was detected in HU. Furthermore, these brines may have been responsible for the addition of Mg, Na, and Ca to HU that were detected by ChemCam and APXS. The Si-sulfate brine mechanism also enables the idea for the placement of magnetite and Fe and Mn veins in HU to occur before SPg placement Gm (Gasda et al., 2022).
6. Subsequent to replacement of unfractionated S with enriched ^{34}S in HU, an additional alteration event occurred that consisted of low S fluids that permitted removal of S resulting in the relatively low S concentration levels that were detected in HU by the SAM-EGA and the APXS instruments (Tables S2 and S5 in Supporting Information S2).
7. Carbon concentrations were not significantly different between the Gm samples, which was consistent with carbon stabilization through adsorption onto amorphous Al- and Fe-hydroxide phases. Minor carbon encapsulated in Mg-sulfate may have been lost when Mg-sulfate was leached during HU alteration.

8. All sediments underwent further erosion resulting in the formation of the Gp capping unit and exposing sediments for sampling by *Curiosity* rover.

5.6. Implications for Habitability

The detection of hydrated phases (e.g., phyllosilicates) as evidence by evolved water detections and evidence of aqueous alteration in the Gm and Gp materials has demonstrated that environmental conditions likely supplied sufficient liquid water that would have enabled microbiologically habitable conditions (e.g., Grotzinger et al., 2014; Losa-Adams et al., 2021). Evidence of greater levels of aqueous alteration in the HU materials was consistent with aqueous alteration processes that could have operated for longer periods. This would have extended habitable conditions along the SPg unconformity over longer periods relative to less altered sediments above and below the contact.

While water and carbon (Table S6 in Supporting Information S2) may have been sufficient in the Gm sediments, the undetectable to very low N levels could have limited heterotrophic microbiology in Gm sediments (Table S8 in Supporting Information S2). The possibility exists that suitable levels of microbially available nitrogen were available through abiotic or possibly biologically mediated N-cycle; however, later diagenetic processes could have leached any evidence of sufficient nitrogen from the Gm mudstones. The non-detection of N cannot be ignored suggesting that Gm mudstones may not, despite evidence of aqueous processes, have provided sufficient N to support even limited microbial populations.

Carbon and N levels in EB (Tables S6 and S8 in Supporting Information S2) may have been sufficient to support heterotrophic microbiology in Sf sediments. Microbially active soils in the Antarctic Dry Valleys have C (320–1,600 $\mu\text{gC/g}$) and N (5–114 $\mu\text{gN/g}$) contents that are similar to what has been detected in the EB sample (Hopkins et al., 2006). Though microbial activity is maintained by influx of detrital organics that serve to replenish C and N lost through heterotrophic processes in these Antarctic soils (Elberling et al., 2006; Hopkins et al., 2006). Provided that C and N levels were replenished by abiotic or biotic inputs and all necessary environmental and other essential geochemical conditions (e.g., pH, redox, and abundance of other essential nutrients) were favorable for life, heterotrophic microbial processes could have been supported by C and N levels in the EB sediments.

Despite the possibility that N levels could have been limiting in regard to the Gm materials, depleted sulfate- $\delta^{34}\text{S}$ in the EB sample and depleted CH_4 - $\delta^{13}\text{C}$ values in both the HU and EB samples are consistent with biological isotope fractionation processes, though abiotic fractionation can also explain such depletions (Franz et al., 2017; House et al., 2022; Wong et al., 2022). This suggests that we cannot necessarily exclude microbiological processes along the SPg unconformity or at least in the source regions where these sediments or dissolved fractionated solutes were derived.

6. Conclusions

Results of SAM-EGA analyses sediments above and below the SPg unconformity have experienced a complex history of aqueous alteration. The HU below the SPg unconformity through either acid or Si-poor brine alteration experienced loss of smectite that transformed to cristobalite/Opal CT and amorphous Fe. Sulfate with an unfractonated $\delta^{34}\text{S}$ signature in HU was replaced with sulfate with an enriched $\delta^{34}\text{S}$ signature. The lack of significant differences in carbon abundances between the more altered HU sample and less altered GG and NT samples suggests that HU alteration processes did not significantly affect C abundance in HU. The HU carbon could exist as adsorbed or insoluble refractory phases and that would have resisted loss from HU alteration. While many abiotic sources of C are possible, SAM-EGA results cannot exclude the possible detection of biotically derived C. Limited nitrate and no oxychlorine in HU as well as throughout all of the GT trough materials (McAdam et al., 2022) demonstrated that either nitrate and oxychlorine were never deposited in sufficient quantities or that some diagenetic process leached these soluble phases before the SPg unconformity formation.

Contrary to evidence of extensive sulfate, nitrate, oxychlorine fluid exchange between the Mf mudstone and Sf sandstone lower down Aeolis Mons (Yen et al., 2017), there was no evidence of fluid exchange between the Gm mudstone and Sf sandstone in the GT region. The minor Fe- and Al-smectite along with evidence of redox disequilibrium as indicated by iron sulfide, sulfate, oxychlorine, and nitrate detections were consistent with limited

aqueous alteration in the Sf sandstone that served to limit fluid interactions between the Gm and Sf materials in the GT region.

The necessary C and N ingredients for life are present in Gale crater. Sufficient C and N levels for microbial processes were detected in the EB sample and may have been present in Gm sediments. However, maintaining C and N at detected levels through abiotic or biotic inputs would have been required to replenish C and N lost through heterotrophic processes.

Enhanced aqueous processes along the SPg unconformity are evident suggests that habitable conditions may have been extended along the unconformity long after lacustrine conditions were no longer present. Isotopic evidence suggests that microbial isotopic fractionation processes may have been active in Gale crater (Franz et al., 2017; House et al., 2022; Wong et al., 2022). While abiotic isotopic fractionation processes can explain depleted sulfate- $\delta^{34}\text{S}$ and CH_4 - $\delta^{13}\text{C}$ values of material along the SPg unconformity, biological isotopic fractionation processes cannot be ruled out (Franz et al., 2017; House et al., 2022; Wong et al., 2022). SAM results from sediments associated with the SPg unconformity in the GT region have demonstrated that existence of past life on Mars remains an open question and that rigorous laboratory analyses of returned Mars samples will likely be required to determine if life ever arose on Mars.

Data Availability Statement

The data presented in this manuscript is archived and publicly available at the NASA's Planetary Data System Geoscience Node (Mahaffy, 2013) (<https://pds-geosciences.wustl.edu/msl/msl-m-sam-4-rdr-11b-v1/>). Data sets used for figure plots can also be found on Harvard Dataverse (Sutter, 2022).

Acknowledgments

The authors are grateful to the engineers and scientists of the MSL Curiosity team, who have made the mission possible and the reported data available. The authors gratefully acknowledge Rafael Navarro-González who passed away on 28 January 2021. Rafael was a friend and valued member of the SAM team who contributed significantly to SAM data interpretation. This work was funded by support from the NASA to the SAM and MSL teams. J.L.E., C.H.H. and A.C.M acknowledge funding support from the NASA ROSES MSL Participating Scientist Program. S.P.S and S.M.R.T acknowledge funding from UK Space Agency Grant ST/S001522/1 and Research England Expanding Excellence in England (E3) fund (Grant code 124.18). R.N.G. acknowledges funding from the Universidad Nacional Autónoma de México (DGAPA-IN109416) and the Consejo Nacional de Ciencia y Tecnología de México (CONACyT 220626). The authors acknowledge the Mastcam and MAHLI operations team at Malin Space Science Systems (MSSS) for producing and providing all Mastcam mosaic and MAHLI images used in this manuscript. The authors are grateful for assistance from Deirdra M. Fey, Marie J. McBride, and Michael A. Ravine who produced the MAHLI images and MAHLI mosaics used in this manuscript. The authors are grateful to Jeff Schroeder of JPL who provided images for Figure 1. The authors would like to thank the JGR editors, Walter Goetz, and an anonymous reviewer for useful comments and edits that significantly improved this manuscript.

References

- Abras, A., Braga, M. M., & Machado, J. C. (1984). Mossbauer study of ferric oxide particles as products of thermal decomposition of iron/III/ benzoate. *Journal of Radioanalytical and Nuclear Chemistry*, 86(2), 111–122. <https://doi.org/10.1007/bf02164907>
- Achilles, C. N., Rampe, E. B., Downs, R. T., Bristow, T. F., Ming, D. W., Morris, R. V., et al. (2020). Evidence for multiple diagenetic episodes in ancient fluvial-lacustrine sedimentary rocks in Gale crater, Mars. *Journal of Geophysical Research: Planets*, 125(8), e2019JE006295. <https://doi.org/10.1029/2019JE006295>
- Altheide, T. S., Chevrier, V. F., & Noe-Dobrea, E. (2010). Mineralogy characterization of acid weathered phyllosilicates with implications for secondary Martian deposits. *Geochimica et Cosmochimica Acta*, 74, 6232–6248. <https://doi.org/10.1016/j.gca.2010.08.005>
- Anderson, R., & Bell, J. F. (2010). Geologic mapping and characterization of Gale Crater and implications for its potential as a Mars Science Laboratory landing site. *The Mars Journal*, 5, 76–128. <https://doi.org/10.1555/mars.2010.0004>
- Applin, D. M., Izawa, M. R. M., Cloutis, E. A., Goltz, D., & Johnson, J. R. (2015). Oxalate minerals on Mars? *Earth and Planetary Science Letters*, 420, 127–139. <https://doi.org/10.1016/j.epsl.2015.03.034>
- Archer, P. D., Franz, H. B., Sutter, B., Arevalo, R. D., Coll, P., Eigenbrode, J. L., et al. (2014). Abundances and implications of volatile-bearing species from evolved gas analysis of the Rocknest aeolian deposit, Gale crater, Mars. *Journal of Geophysical Research: Planets*, 119(1), 237–254. <https://doi.org/10.1002/2013JE004493>
- Aubrey, A., Cleaves, H. J., Chalmers, J. H., Skelley, A. M., Mathies, R. A., Grunthaner, F. J., et al. (2006). Sulfate minerals and organic compounds on Mars. *Geology*, 34(5), 357–360. <https://doi.org/10.1130/g22316.1>
- Baker, L. L., & Neill, O. K. (2017). Geochemistry and mineralogy of a saprolite developed on Columbia River Basalt: Secondary clay formation, element leaching, and mass balance during weathering. *American Mineralogist*, 102(8), 1623–1645. <https://doi.org/10.2138/am-2017-5964>
- Banham, S. G., Gupta, S., Rubin, D. M., Bedford, C. C., Edgar, L. A., Bryk, A. B., et al. (2022). Evidence for fluctuating wind in shaping an ancient Martian dune field: The Stimson formation at the Greenheugh pediment, Gale crater. *Journal of Geophysical Research: Planets*, 127(9), e2021JE007023. <https://doi.org/10.1029/2021JE007023>
- Banham, S. G., Gupta, S., Rubin, D. M., Edgett, K. S., Barnes, R., Van Beek, J., et al. (2021). A rock record of complex aeolian bedforms in a Hesperian Desert Landscape: The Stimson formation as exposed in the Murray buttes, Gale crater, Mars. *Journal of Geophysical Research: Planets*, 126(4), e2020JE006554. <https://doi.org/10.1029/2020je006554>
- Banham, S. G., Gupta, S., Rubin, D. M., Watkins, J. A., Sumner, D. Y., Edgett, K. S., et al. (2018). Ancient Martian aeolian processes and palaeomorphology reconstructed from the Stimson formation on the lower slope of Aeolis Mons, Gale crater, Mars. *Sedimentology*, 65(4), 993–1042. <https://doi.org/10.1111/sed.12469>
- Bedford, C. C., Banham, S. G., Bridges, J. C., Forni, O., Cousin, A., Bowden, D., et al. (2022). An insight into ancient aeolian processes and post-Noachian aqueous alteration in Gale crater, Mars, using ChemCam geochemical data from the Greenheugh capping unit. *Journal of Geophysical Research: Planets*, 127(9), e2021JE007100. <https://doi.org/10.1029/2021JE007100>
- Bedford, C. C., Schwenzer, S. P., Bridges, J. C., Banham, S., Wiens, R. C., Gasnault, O., et al. (2020). Geochemical variation in the Stimson formation of Gale crater: Provenance, mineral sorting, and a comparison with modern Martian dunes. *Icarus*, 341, 113622. <https://doi.org/10.1016/j.icarus.2020.113622>
- Benner, S. A., Devine, K. G., Matveeva, L. N., & Powell, D. H. (2000). The missing organic molecules on Mars. *Proceedings of the National Academy of Sciences of the United States of America*, 97(6), 2425–2430. <https://doi.org/10.1073/pnas.040539497>
- Bennett, K. A., Fox, V. K., Bryk, A., Dietrich, W., Fedo, C., Edgar, L., et al. (2022). The Curiosity rover's exploration of Glen Torridon, Gale crater, Mars: An overview of the Campaign and scientific results. *Journal of Geophysical Research: Planets*, 127, e2022JE007185. <https://doi.org/10.1029/2022JE007185>

- Benson, L. V., & Teague, L. S. (1982). Diagenesis of basalts from the Pasco Basin, Washington-I. Distribution and composition of secondary mineral phases. *Journal of Sedimentary Petrology*, 52, 595–613. <https://doi.org/10.1306/212F7FAE-2B24-11D7-8648000102C1865D>
- Bish, D. L., Blake, D. F., Vaniman, D. T., Chipera, S. J., Morris, R. V., Ming, D. W., et al. (2013). X-ray diffraction results from Mars Science Laboratory: Mineralogy of Rocknest at Gale crater. *Science*, 341(6153), 341. <https://doi.org/10.1126/science.1238932>
- Blake, D. F., Morris, R. V., Kocurek, G., Morrison, S. M., Downs, R. T., Bish, D., et al. (2013). Curiosity at Gale crater, Mars: Characterization and analysis of the Rocknest sand shadow. *Science*, 341(6153), 341. <https://doi.org/10.1126/science.1239505>
- Boily, J. F., Szanyi, J., & Felmy, A. R. (2007). Effects of surface coordination on the temperature-programmed desorption of oxalate from goethite. *Journal of Physical Chemistry*, 111(45), 17072–17081. <https://doi.org/10.1021/jp075576q>
- Bristow, T. F., Grotzinger, J. P., Rampe, E. B., Cuadros, J., Chipera, S. J., Downs, G. W., et al. (2021). Brine-driven destruction of clay minerals in Gale crater, Mars. *Science*, 373(6551), 198–204. <https://doi.org/10.1126/science.abg5449>
- Cannon, K. M., Sutter, B., Ming, D. W., Boynton, W. V., & Quinn, R. (2012). Perchlorate induced low temperature carbonate decomposition in the Mars Phoenix Thermal and Evolved Gas Analyzer (TEGA). *Geophysical Research Letters*, 39(13), L13203. <https://doi.org/10.1029/2012GL051952>
- Clara, C., Sciana, A. N., & Aglietti, E. F. (2003). Synthesis and characterization of aluminum carboxylate gels. *Thermochimica Acta*, 407(1–2), 33–40. [https://doi.org/10.1016/S0040-6031\(03\)00265-X](https://doi.org/10.1016/S0040-6031(03)00265-X)
- Clark, J., Sutter, B., Archer, P. D., Jr., Ming, D., Rampe, E., McAdam, A., et al. (2021). A review of Sample Analysis at Mars-Evolved Gas Analysis Laboratory analog work supporting the presence of perchlorates and chlorates in Gale crater, Mars. *Minerals*, 11(5), 475. <https://doi.org/10.3390/min11050475>
- Clark, J. V., Sutter, B., McAdam, A. C., Rampe, E. B., Archer, P. D., Ming, D. W., et al. (2020). High-temperature HCl evolutions from mixtures of perchlorates and chlorides with water-bearing phases: Implications for the SAM instrument in Gale crater, Mars. *Journal of Geophysical Research: Planets*, 125(2), e2019JE006173. <https://doi.org/10.1029/2019JE006173>
- Dehouck, E., Cousin, A., Mangold, N., Frydenvang, J., Gasnault, O., Forni, O., et al. (2022). Bedrock geochemistry and alteration history of the clay-bearing Glen Torridon region of Gale crater, Mars. *Journal of Geophysical Research: Planets*, 127, e2021JE007103. <https://doi.org/10.1029/2021JE007103>
- Dollimore, D. (1987). The thermal decomposition of oxalates. A review. *Thermochimica Acta*, 117, 331–363. [https://doi.org/10.1016/0040-6031\(87\)88127-3](https://doi.org/10.1016/0040-6031(87)88127-3)
- Dollimore, D., & Griffiths, D. L. (1970). Differential thermal analysis study of various oxalates in oxygen and nitrogen. *Journal of Thermal Analysis*, 2(3), 229–250. <https://doi.org/10.1007/bf01911405>
- Egli, M., Nater, M., Mirabella, A., Raimondi, S., Plötze, M., & Alioth, L. (2008). Clay minerals, oxyhydroxide formation, element leaching and humus development in volcanic soils. *Geoderma*, 143(1–2), 101–104. <https://doi.org/10.1016/j.geoderma.2007.10.020>
- Eigenbrode, J. L., Bower, H., & Archer, P., Jr. (2014). Decarboxylation of carbon compounds as a potential source for CO₂ and CO observed by SAM at Yellowknife Bay, Gale crater, Mars. In *Proceedings of the 45th Lunar and Planetary Science Conference, #1605*. Lunar and Planetary Institute.
- Eigenbrode, J. L., Summons, R. E., Steele, A., Freissinet, C., Millan, M., Navarro-Gonzalez, R., et al. (2018). Organic matter preserved in 3-billion-year-old mudstones at Gale crater, Mars. *Science*, 360(6393), 1096–1100. <https://doi.org/10.1126/science.aas9185>
- Elberling, B., Gregorich, E. G., Hopkins, D. W., Sparrow, A. D., Novis, P., & Greenfield, L. G. (2006). Distribution and dynamics of soil organic matter in an Antarctic dry valley. *Soil Biology and Biochemistry*, 38(10), 3095–3106. <https://doi.org/10.1016/j.soilbio.2005.12.011>
- Farley, K. A., Stack, K. M., Shuster, D. L., Horgan, B. H. N., Hurowitz, J. A., Tarnas, J. D., et al. (2022). Aqueously altered igneous rocks sampled on the floor of Jezero crater, Mars. *Science*, 377, 6614. <https://doi.org/10.1126/science.abo2196>
- Fedo, C. M., Bryk, A. B., Edgar, L. A., Bennett, K. A., Fox, V. K., Dietrich, W. E., et al. (2022). Geology and stratigraphic correlation of the Murray and Carolyn Shoemaker formations across the Glen Torridon region, Gale crater, Mars. *Journal of Geophysical Research: Planets*, 127(9), e2022JE007408. <https://doi.org/10.1029/2022JE007408>
- Filimonova, S., Kaufhold, S., Wagner, F. E., Häusler, W., & Kögel-Knabner, I. (2016). The role of allophane nano-structure and Fe-oxide speciation for hosting soil organic matter in an allophanic Andosol. *Geochimica et Cosmochimica Acta*, 180, 284–302. <https://doi.org/10.1016/j.gca.2016.02.033>
- Fisher, G. B., & Ryan, P. C. (2006). The smectite-to-disordered kaolinite transition in tropical soil chronosequence, Pacific Coast, Costa Rica. *Clays and Clay Minerals*, 54(5), 571–586. <https://doi.org/10.1346/ccmn.2006.0540504>
- Flynn, G. J. (1996). The delivery of organic matter from asteroids and comets to the early surface of Mars. *Earth, Moon, and Planets*, 72(1–3), 469–474. <https://doi.org/10.1007/BF00117551>
- Forni, O., Dehouck, E., Cousin, A., Bedford, C. C., & David, G. (2021). Elevated fluorine abundances below the Siccar point unconformity: Implications for fluid Circulation in Gale Crater. In *Presented at the 52nd Lunar and Planetary Science Conference, Abstract 1503*.
- Forni, O., Meslin, P.-Y., Drouet, C., Cousin, A., & David, G. (2020). Apatites in Gale crater. In *Presented at the 51st Lunar and Planetary Science Conference, Abstract 2192*.
- Fox, A. C., Eigenbrode, J. L., & Freeman, K. H. (2019). Radiolysis of macromolecular organic material in Mars-relevant mineral matrices. *Journal of Geophysical Research: Planets*, 124(12), 3257–3266. <https://doi.org/10.1029/2019JE006072>
- Fraeman, A. A., Edgar, L. A., Rampe, E. B., Thompson, L. M., Frydenvang, J., Fedo, C. M., et al. (2020). Evidence for a diagenetic origin of Vera Rubin ridge, Gale crater, Mars: Summary and synthesis of Curiosity's Exploration Campaign. *Journal of Geophysical Research: Planets*, 125(12), e2020JE006527. <https://doi.org/10.1029/2020JE006527>
- Francois, P., Szopa, C., Buch, A., Coll, P., McAdam, A. C., Mahaffy, P. R., et al. (2016). Magnesium sulfate as a key mineral for the detection of organic molecules on Mars using pyrolysis. *Journal of Geophysical Research: Planets*, 121(1), 61–74. <https://doi.org/10.1002/2015JE004884>
- Franz, H. B., McAdam, A. C., Ming, D. W., Freissinet, C., Mahaffy, P. R., Eldridge, D. L., et al. (2017). Large sulfur isotope fractionations in Martian sediments at Gale crater. *Nature Geoscience*, 10(9), 658–662. <https://doi.org/10.1038/NGEO3002>
- Freissinet, C., Glavin, D. P., Mahaffy, P. R., Miller, K. E., Eigenbrode, J. L., Summons, R. E., et al. (2015). Organic molecules in the Sheepbed mudstone, Gale crater, Mars. *Journal of Geophysical Research: Planets*, 120(3), 495–514. <https://doi.org/10.1002/2014JE004737>
- Freissinet, C., Knudson, C. A., Graham, H. V., Lewis, J. M. T., Lasue, J., McAdam, A. C., et al. (2020). Benzoic acid as the preferred precursor for the chlorobenzene detected on Mars: Insights from the unique Cumberland analog investigation. *The Planetary Science Journal*, 1(2), 41. <https://doi.org/10.3847/PSJ/aba690>
- Frydenvang, J., Gasda, P. J., Hurowitz, J. A., Grotzinger, J. P., Wiens, R. C., Newsom, H. E., et al. (2017). Diagenetic silica enrichment and late-stage groundwater activity in Gale crater, Mars. *Geophysical Research Letters*, 44(10), 4716–4724. <https://doi.org/10.1002/2017GL073323>
- Furuichi, R., Ishi, T., & Kobayashi, K. (1974). Phenomenological study of the catalytic thermal decomposition of potassium perchlorate by iron (II) oxides with different preparing histories. *Journal of Thermal Analysis*, 6(3), 305–320. <https://doi.org/10.1007/bf01950062>

- Gainey, S. R., Hausrath, E. M., Hurowitz, J. A., & Milliken, R. E. (2014). Nontronite dissolution rates and implications for Mars. *Geochimica et Cosmochimica Acta*, 126, 192–211. <https://doi.org/10.1016/j.gca.2013.10.055>
- Gasda, P. J., Comellas, J., Essunfeld, A., Das, D., Bryk, A. B., Dehouck, E., et al. (2022). Overview of the morphology and chemistry of diagenetic features in the clay-rich Glen Torridon unit of Gale crater, Mars. *Journal of Geophysical Research: Planets*, 127, e2021JE007097. <https://doi.org/10.1029/2021JE007097>
- Gates, W. P., Anderson, J. S., Raven, M. D., & Churchman, G. J. (2002). Mineralogy of a bentonite from Miles, Queensland, Australia and characterisation of its acid activation products. *Applied Clay Science*, 20(4–5), 189–197. [https://doi.org/10.1016/s0169-1317\(01\)00072-2](https://doi.org/10.1016/s0169-1317(01)00072-2)
- Glavin, D. P., Freissinet, C., Miller, K. E., Eigenbrode, J. L., Brunner, A. E., Buch, A., et al. (2013). Evidence for perchlorates and the origin of chlorinated hydrocarbons detected by SAM at the Rocknest aeolian deposit in Gale Crater. *Journal of Geophysical Research: Planets*, 118(10), 1955–1973. <https://doi.org/10.1002/jgre.20144>
- Grotzinger, J. P., Gupta, S., Malin, M. C., Rubin, D. M., Schieber, J., Siebach, K., et al. (2015). Deposition, exhumation, and paleoclimate of an ancient lake deposit, Gale crater, Mars. *Science*, 350(6257), 350. <https://doi.org/10.1126/science.aac7575>
- Grotzinger, J. P., Sumner, D. Y., Kah, L. C., Stack, K., Gupta, S., Edgar, L., et al. (2014). A habitable fluvio-lacustrine environment at Yellowknife Bay, Gale crater, Mars. *Science*, 343(6169), 343. <https://doi.org/10.1126/science.1242777>
- Hogancamp, J. V., Sutter, B., Morris, R. V., Archer, P. D., Ming, D. W., Rampe, E. B., et al. (2018). Chlorate/Fe-bearing phase mixtures as a possible source of oxygen and chlorine detected by the Sample Analysis at Mars instrument in Gale crater, Mars. *Journal of Geophysical Research: Planets*, 123(11), 2920–2938. <https://doi.org/10.1029/2018JE005691>
- Hopkins, D. W., Sparrow, A. D., Elberling, B., Gregorich, E. G., Novis, P. M., Greenfield, L. G., & Tilston, E. L. (2006). Carbon, nitrogen and temperature controls on microbial activity in soils from an Antarctic dry valley. *Soil Biology and Biochemistry*, 38(10), 3130–3140. <https://doi.org/10.1016/j.soilbio.2006.01.012>
- Horgan, B. H. N., Johnson, J. R., Fraeman, A. A., Rice, M. S., Seeger, C., Bell, J. F., III, et al. (2020). Diagenesis of Vera Rubin ridge, Gale crater, Mars, from Mastcam multispectral images. *Journal of Geophysical Research: Planets*, 125(11), e2019JE006322. <https://doi.org/10.1029/2019JE006322>
- Hoshino, Y., Utsunomiya, T., & Abe, O. (1981). The thermal decomposition of sodium nitrate and the effects of several oxides on the decomposition. *Bulletin of the Chemical Society of Japan*, 54(5), 1385–1391. <https://doi.org/10.1246/bcsj.54.1385>
- House, C. H., Wong, G. M., Webster, C. R., Flesch, G. J., Franz, H. B., Stern, J. C., et al. (2022). Depleted carbon isotope compositions observed at Gale crater, Mars. *Proceedings of the National Academy of Sciences*, 119(4), e2115651119. <https://doi.org/10.1073/pnas.2115651119>
- Jewur, S. S., & Kuriacose, J. C. (1977). Studies on the thermal decomposition of ferric acetate. *Thermochimica Acta*, 19(2), 195–200. [https://doi.org/10.1016/0040-6031\(77\)85107-1](https://doi.org/10.1016/0040-6031(77)85107-1)
- Judd, M. D., Plunkett, B. A., & Pope, M. I. (1974). The thermal decomposition of calcium, sodium, silver and copper (II) acetates. *Journal of Thermal Analysis*, 6(5), 555–563. <https://doi.org/10.1007/bf01911560>
- Lewis, J. M. T., Eigenbrode, J. L., Wong, G. M., McAdam, A. C., Archer, P. D., Sutter, B., et al. (2021). Pyrolysis of oxalate, acetate, and perchlorate mixtures and the implications for organic salts on Mars. *Journal of Geophysical Research: Planets*, 126(4), e2020JE006803. <https://doi.org/10.1029/2020JE006803>
- Lewis, J. M. T., Watson, J. S., Najorka, J., Luong, D., & Sephton, M. A. (2015). Sulfate minerals: A problem for the detection of organic compounds on Mars? *Astrobiology*, 15(3), 247–258. <https://doi.org/10.1089/ast.2014.1160>
- Losa-Adams, E., Gill-Lozano, C., Fairen, A. G., Bishop, J. L., Rampe, E. B., & Gago-Duport, L. (2021). Long-lasting habitable periods in Gale crater constrained by glauconitic clays. *Nature Astronomy*, 5(9), 936–942. <https://doi.org/10.1038/s41550-021-01397-x>
- Macpherson, C. G., Hilton, D. R., Newman, S., & Matthey, D. P. (1999). CO₂, ¹³C/¹²C and H₂O variability in natural basaltic glasses: A study comparing stepped heating and FTIR spectroscopic techniques. *Geochimica et Cosmochimica Acta*, 63(11–12), 1805–1813. [https://doi.org/10.1016/s0016-7037\(99\)00124-6](https://doi.org/10.1016/s0016-7037(99)00124-6)
- Mahaffy, P. R. (2013). MSL Mars sample analysis at Mars 4 RDR level 1B V1.0 [Dataset]. NASA Planetary Data System. <https://doi.org/10.17189/1519446>
- Mahaffy, P. R., Webster, C. R., Cabane, M., Conrad, P. G., Coll, P., Atreya, S. K., et al. (2012). The sample analysis at Mars investigation and instrument suite. *Space Science Reviews*, 170(1–4), 401–478. <https://doi.org/10.1007/s11214-012-9879-z>
- Manning, C. V., Zahnle, K. J., & McKay, C. P. (2009). Impact processing of nitrogen on early Mars. *Icarus*, 199(2), 273–285. <https://doi.org/10.1016/j.icarus.2008.10.015>
- McAdam, A. C., Franz, H. B., Sutter, B., Archer, P. D., Jr., Freissinet, C., Eigenbrode, J. L., et al. (2014). Sulfur-bearing phases detected by evolved gas analysis of the Rocknest aeolian deposit, Gale Crater, Mars. *Journal of Geophysical Research: Planets*, 119(2), 373–393. <https://doi.org/10.1002/2013JE004518>
- McAdam, A. C., Sutter, B., Archer, P. D., Franz, H. B., Wong, G. M., Lewis, J. M. T., et al. (2020). Constraints on the mineralogy and geochemistry of Vera Rubin ridge, Gale crater, Mars, from Mars Science Laboratory Sample Analysis at Mars evolved gas analyses. *Journal of Geophysical Research: Planets*, 125(11), e2019JE006309. <https://doi.org/10.1029/2019JE006309>
- McAdam, A. C., Sutter, B., Archer, P. D., Franz, H. B., Wong, G. M., Lewis, J. M. T., et al. (2022). Evolved gas analyses of sedimentary rocks from the Glen Torridon clay-bearing unit, Gale crater, Mars: Results from the Mars Science Laboratory Sample Analysis at Mars instrument suite. *Journal of Geophysical Research: Planets*, 127(9), e2022JE007179. <https://doi.org/10.1029/2022JE007179>
- McKinley, J. M., Worden, R. H., & Ruffell, A. H. (2003). Smectite in sandstones: A review of the controls on occurrence and behaviour during diagenesis. *International Association of Sedimentologists Special Publication*, 34, 109–128.
- Millan, M., Williams, A. J., McAdam, A. C., Eigenbrode, J. L., Steele, A., Freissinet, C., et al. (2022). Sedimentary organics in Glen Torridon, Gale crater, Mars: Results from the SAM instrument suite and supporting laboratory analyses. *Journal of Geophysical Research: Planets*, 127, e2021JE007107. <https://doi.org/10.1029/2021JE007107>
- Milliken, R. E., Grotzinger, J. P., & Thomson, B. J. (2010). Paleoclimate of Mars as captured by the stratigraphic record in Gale crater: Stratigraphy of Gale crater. *Geophysical Research Letters*, 37(4), L04201. <https://doi.org/10.1029/2009GL041870>
- Mohamed, M. A., Galwey, A. K., & Halawy, S. A. (2002). The activities of some metal oxides in promoting the thermal decomposition of potassium oxalate. *Thermochimica Acta*, 387(1), 63–74. [https://doi.org/10.1016/s0040-6031\(01\)00830-9](https://doi.org/10.1016/s0040-6031(01)00830-9)
- Nachon, M., Mangold, N., Forni, O., Kah, L. C., Cousin, A., Wiens, R. C., et al. (2017). Chemistry of diagenetic features analyzed by ChemCam at Pahrump Hills, Gale crater, Mars. *Icarus*, 281, 121–136. <https://doi.org/10.1016/j.icarus.2016.08.026>
- NIST Standard Reference Database 69. (2021). NIST chemistry WebBook. <https://doi.org/10.18434/T4D303>
- O'Connell-Cooper, C. D., Thompson, L. M., Spray, J. G., Berger, J. A., Gellert, R., McCraig, M., et al. (2022). Statistical analysis of APXS-derived chemistry of the clay-bearing Glen Torridon region and Mount Sharp group, Gale crater, Mars. *Journal of Geophysical Research: Planets*, 127(9), e2021JE007177. <https://doi.org/10.1029/2021JE007177>

- Okumura, F., & Mimura, K. (2011). Gradual and stepwise pyrolyses of insoluble organic matter from the Murchison meteorite revealing chemical structure and isotopic distribution. *Geochimica et Cosmochimica Acta*, 75(22), 7063–7080. <https://doi.org/10.1016/j.gca.2011.09.015>
- Pavlov, A. A., Vasilyev, G., Ostryakov, V. M., Pavlov, A. K., & Mahaffy, P. (2012). Degradation of the organic molecules in the shallow subsurface of Mars due to irradiation by cosmic rays. *Geophysical Research Letters*, 39(13), L13202. <https://doi.org/10.1029/2012gl052166>
- Pineau, F., & Javoy, M. (1994). Strong degassing at ridge crests: The behaviour of dissolved carbon and water in basalt glasses at 14°N, Mid-Atlantic Ridge. *Earth and Planetary Science Letters*, 123(1–3), 179–198. [https://doi.org/10.1016/0012-821x\(94\)90266-6](https://doi.org/10.1016/0012-821x(94)90266-6)
- Rampe, E. B., Bristow, T. F., Morris, R. V., Morrison, S. M., Achilles, C. N., Ming, D. W., et al. (2020). Mineralogy of Vera Rubin ridge from the Mars Science Laboratory CheMin instrument. *Journal of Geophysical Research: Planets*, 125(9), e2019JE006306. <https://doi.org/10.1029/2019JE006306>
- Rampe, E. B., Lapotre, M. G. A., Bristow, T. F., Arvidson, R. E., Morris, R. V., Achilles, C. N., et al. (2018). Sand mineralogy within the Bagnold Dunes, Gale crater, as observed in situ and from orbit. *Geophysical Research Letters*, 45(18), 45–9497. <https://doi.org/10.1029/2018GL079073>
- Rampe, E. B., Ming, D. W., Blake, D. F., Bristow, T. F., Chipera, S. J., Grotzinger, J. P., et al. (2017). Mineralogy of an ancient lacustrine mudstone succession from the Murray formation, Gale crater, Mars. *Earth and Planetary Science Letters*, 471, 172–185. <https://doi.org/10.1016/j.epsl.2017.04.021>
- Remusat, L., Derenne, S., Robert, F., & Knicker, H. (2005). New pyrolytic and spectroscopic data on Orgueil and Murchison insoluble organic matter: A different origin than soluble? *Geochimica et Cosmochimica Acta*, 60(15), 3919–3932. <https://doi.org/10.1016/j.gca.2005.02.032>
- Robert, F., & Epstein, S. (1982). The concentration and isotopic composition of hydrogen, carbon and nitrogen in carbonaceous meteorites. *Geochimica et Cosmochimica Acta*, 46(1), 81–95. [https://doi.org/10.1016/0016-7037\(82\)90293-9](https://doi.org/10.1016/0016-7037(82)90293-9)
- Rudloff, W. K., & Freeman, E. S. (1970). Catalytic effect of metal oxides on thermal decomposition reactions. II. The catalytic effect of metal oxides on the thermal decomposition of potassium chlorate and potassium perchlorate as detected by thermal analysis methods. *Journal of Physical Chemistry*, 74(18), 3317–3324. <https://doi.org/10.1021/j100712a002>
- Rudolph, A., Horgan, B., Johnson, J., Bennett, K., Haber, J., Bell, J. F., III, et al. (2022). The distribution of clay minerals and their impact on diagenesis in Glen Torridon, Gale crater, Mars. *Journal of Geophysical Research: Planets*, 127(10), e2021JE007098. <https://doi.org/10.1029/2021JE007098>
- Ryan, P. C., & Huertas, F. J. (2009). The temporal evolution of pedogenic Fe–smectite to Fe–kaolin via interstratified kaolin–smectite in a moist tropical soil chronosequence. *Geoderma*, 151(1–2), 1–15. <https://doi.org/10.1016/j.geoderma.2009.03.010>
- Segura, A., & Navarro-González, R. (2005). Nitrogen fixation on early Mars by volcanic lightning and other sources. *Geophysical Research Letters*, 32(5), L05203. <https://doi.org/10.1029/2004gl021910>
- Sharp, J. H., Wilburn, F. W., & McIntosh, R. M. (1991). The effect of procedural variables on TG, DTG and DTA curves of magnesite and dolomite. *Journal of Thermal Analysis and Calorimetry*, 37, 2021–2029.
- Sherman, G. D., Ikawa, H., Uehara, G., & Okazaki, E. (1962). Types of occurrence of nontronite and nontronite-like minerals in soils. *Pacific Science*, 16, 57–62.
- Sposito, G. (1989). *The chemistry of soils* (pp. 61 (277)). Oxford University Press.
- Steele, A., Benning, L. G., Wirth, R., Siljeström, S., Fries, M. D., Hauri, E., et al. (2018). Organic synthesis on Mars by electrochemical reduction of CO₂. *Science Advances*, 4(10), eaat5118. <https://doi.org/10.1126/sciadv.aat5118>
- Steele, A., McCubbin, F. M., Fries, M., Kater, L., Boctor, N. Z., Fogel, M. L., et al. (2012). A reduced organic carbon component in Martian basalts. *Science*, 337(6091), 212–215. <https://doi.org/10.1126/science.1220715>
- Steele, A., McCubbin, F. M., & Fries, M. D. (2016). The provenance, formation, and implications of reduced carbon phases in Martian meteorites. *Meteoritics & Planetary Science*, 51(11), 2203–2225. <https://doi.org/10.1111/maps.12670>
- Stern, J. C., Malespin, C. A., Eigenbrode, J. L., Webster, C. R., Flesch, G. J., Franz, H. B., et al. (2022). Organic carbon concentrations in 3-billion-year-old lacustrine mudstones of Mars. *Proceedings of the National Academy of Sciences*, 119(27), e2201139119. <https://doi.org/10.1073/pnas.2201139119>
- Stern, J. C., Sutter, B., Jackson, W. A., Navarro-González, R., McKay, C. P., Ming, D. W., et al. (2017). The nitrate/perchlorate relationship on Mars. *Geophysical Research Letters*, 44(6), 2643–2651. <https://doi.org/10.1002/2016GL072199>
- Stern, J. S., Sutter, B., Freissinet, C., Navarro-González, R., McKay, C. P., Archer, P. D., Jr., et al. (2015). Evidence for indigenous nitrogen in sedimentary and aeolian deposits from the Curiosity rover investigations at Gale crater, Mars. *Proceedings of the National Academy of Sciences of the United States of America*, 112, 4245–4425. <https://doi.org/10.1073/pnas.1420932112>
- Summers, D. P., & Khare, B. (2007). Nitrogen fixation on early Mars and other terrestrial planets: Experimental demonstration of abiotic fixation reactions to nitrite and nitrate. *Astrobiology*, 7(2), 333–341. <https://doi.org/10.1089/ast.2006.0032>
- Sutter, B. (2022). *Siccar Point group unconformity SAM-EGA data*. Harvard Dataverse. <https://doi.org/10.7910/DVN/WJTR2R>
- Sutter, B., McAdam, A. C., Mahaffy, P. R., Ming, D. W., Edgett, K. S., Rampe, E. B., et al. (2017). Evolved gas analyses of sedimentary rocks and eolian sediment in Gale crater, Mars: Results of the Curiosity rover's sample analysis at Mars instrument from Yellowknife Bay to the Namib Dune. *Journal of Geophysical Research: Planets*, 122(12), 2574–2609. <https://doi.org/10.1002/2016JE005225>
- Thompson, L. M., Spray, J. G., O'Connell-Cooper, C., Berger, J. A., Yen, A., Gellert, R., et al. (2022). Alteration at the base of the Siccar Point unconformity and further evidence for an alkaline provenance at Gale crater: Exploration of the Mount Sharp group, Greenheugh pediment cap rock contact with APXS. *Journal of Geophysical Research: Planets*, 127(11), e2021JE007178. <https://doi.org/10.1029/2021JE007178>
- Thorpe, M. T., Bristow, T. F., Rampe, E. B., Tosca, N. J., Grotzinger, J. P., Bennett, K. A., et al. (2022). Mars Science Laboratory CheMin data from the Glen Torridon region and the significance of lake-groundwater interactions in interpreting mineralogy and sedimentary history. *Journal of Geophysical Research: Planets*, 127(11), e2021JE007099. <https://doi.org/10.1029/2021JE007099>
- Treiman, A. H., Bish, D. L., Vaniman, D. T., Chipera, S. J., Blake, D. F., Ming, D. W., et al. (2016). Mineralogy, provenance, and diagenesis of a potassic basaltic sandstone on Mars: CheMin X-ray diffraction of the Windjana sample (Kimberley area, Gale crater). *Journal of Geophysical Research: Planets*, 121(1), 75–106. <https://doi.org/10.1002/2015JE004932>
- Vingiani, S., Righi, D., Petit, S., & Terribile, F. (2004). Mixed-layer kaolinite-smectite minerals in a red-black soil sequence from basalt in Sardinia (Italy). *Clays and Clay Minerals*, 52(4), 473–483. <https://doi.org/10.1346/ccmn.2004.0520408>
- Vlase, T., Vlase, G., & Doca, N. (2005). Thermal stability of food additives of glutamate and benzoate type. *Journal of Thermal Analysis and Calorimetry*, 80(2), 425–428. <https://doi.org/10.1007/s10973-005-0671-0>
- Williams, A., Eigenbrode, J., Millan, M., Williams, R., Buch, A., Teinturier, S., et al. (2021). Organic molecules detected with the first TMAH wet chemistry experiment, Gale Crater, Mars. In *Lunar and Planetary Science Conference* (pp. 1763).
- Wong, G. M., Franz, H. B., Clark, J. V., McAdam, A. C., Lewis, J. M. T., Millan, M., et al. (2022). Oxidized and reduced sulfur observed by the Sample Analysis at Mars (SAM) instrument suite on the Curiosity rover within the Glen Torridon region at Gale crater, Mars. *Journal of Geophysical Research: Planets*, 127(9), e2021JE007084. <https://doi.org/10.1029/2021JE007084>

- Worden, R. H., & Morad, S. (2003). Clay minerals in sandstones: Controls on formation, distribution and evolution. *International Association of Sedimentologists Special Publication*, 34, 3–41.
- Yen, A. S., Ming, D. W., Vaniman, D. T., Gellert, R., Blake, D. F., Morris, R. V., et al. (2017). Multiple stages of aqueous alteration along fractures in mudstone and sandstone strata in Gale crater, Mars. *Earth and Planetary Science Letters*, 471, 186–198. <https://doi.org/10.1016/j.epsl.2017.04.033>
- Yen, A. S., Morris, R. V., Ming, D. W., Schwenzer, S. P., Sutter, B., Vaniman, D. T., et al. (2021). Formation of tridymite and evidence for a hydrothermal history at Gale crater, Mars. *Journal of Geophysical Research: Planets*, 126(3), e2020JE006569. <https://doi.org/10.1029/2020JE006569>

References From the Supporting Information

- Rice, M. S., Gupta, S., Treiman, A. H., Stack, K. M., Calef, F., Edgar, L. A., et al. (2017). Geologic overview of the Mars Science Laboratory rover mission at the Kimberley, Gale crater, Mars. *Journal of Geophysical Research: Planets*, 122(1), 2–20. <https://doi.org/10.1002/2016JE005200>